Doctor thesis

(2019)

Enhanced hexosamine signaling in aggressive breast cancer

Implications of metabolic and signaling networks involving hyaluronan production and *O*-GlcNAcylation

Kyoto Sangyo University Graduate School

Division of Life Science

Doctor course, 4th year

659073

Chatchadawalai Chokchaitaweesuk

Abstract

The hexosamine biosynthetic pathway (HBP) metabolically regulates dynamic cellular events by linking nutrient availability to numerous signaling networks. Significant alterations in the HBP are often associated with cancer pathogenesis. In this study, I investigated the molecular events underlying cancer pathogenesis associated with enhanced HBP flux. Multidimensional analysis of microarray datasets demonstrated up-regulation of genes encoding HBP enzymes in clinical breast cancers and revealed that co-expression of hyaluronan synthase 2 (HAS2) and glutamine:fructose-6-phosphate amidotransferase (GFAT), a rate limiting enzyme of the HBP, was strongly correlated with a poor prognosis in advanced cancer patients. Consistently with the clinical data, comparative analyses of distinct breast cancer mouse models demonstrated enhancement of the HBP gene expression in primary carcinoma cells, with elevation of Has2 expression and hyaluronan production in aggressive breast cancer cells. The silencing of GFAT reduced $CD44^{high}/CD24^{low}$ cancer stem cell (CSC)-like subpopulations, aldehyde dehydrogenase-positive cell populations, and mammosphere size, which were further diminished by gene targeting of Has2. *Has2* gene disruption reduced the *in vivo* growth of aggressive cancer cells and attenuated pro-tumorigenic Akt/GSK3β/β-catenin signaling and cisplatin resistance. Overall protein *O*-GlcNAcylation was also elevated in association with HBP enhancement in aggressive cancer cells, and the modification exhibited overlapping but distinct roles from the hyaluronan signal in the regulation of CSC-like features. The current data therefore demonstrate that enhanced hexosamine metabolism drives pro-tumorigenic signaling pathways involving hyaluronan and *O*-GlcNAcylation in aggressive breast cancer.

Table of Contents

Introduction

Cancer cells reprogram metabolic pathways to optimally meet their energy and nutrient requirements. The most prominent metabolic alterations in cancer are an increase in glucose uptake and elevation of aerobic glycolysis, termed the Warburg effect (Warburg, 1956; Vander Heiden *et al*., 2009). With recent advances in metabolomics, the understanding of how metabolic reprogramming is linked to malignant transformation has expanded greatly (Soga, 2013; Bruntz *et al*., 2017). Emerging evidence has also shown that metabolic shifts are an important factor in sustaining the self-renewing state of cancer stem cells (CSCs) responsible for tumor initiation, growth, and recurrence (Dong *et al*., 2013; Menendez *et al*., 2013; Ito and Suda, 2014). To date, however, there is limited knowledge on how the interplay between metabolic and signaling networks governs cancer development and progression.

The nutrient-sensing hexosamine biosynthetic pathway (HBP) is a glucose metabolic pathway branching off from main glycolysis (Figure 1) (Taparra *et al*., 2016). The HBP synthesizes uridine diphosphate-*N*-acetylglucosamine (UDP-GlcNAc), which serves as a key metabolite essential for multiple protein glycosylations, glycosaminoglycan biosynthesis, and cellular signaling through protein *O*-GlcNAcylation. *O*-GlcNAcylation is a post-translational modification that transfers a single *O*-GlcNAc moiety from UDP-GlcNAc to serine/threonine residues of proteins (Hart, 2014; Bond and Hanover, 2015). *O*-GlcNAcylation is tightly regulated by the *O*-GlcNAc cycling enzymes *O*-GlcNAc transferase (OGT) and *O*-GlcNAcase (OGA) (Figure 2). The modification occurs in a wide spectrum of intracellular proteins and regulates various distinct cellular processes, including transcription, translation, signal transduction, epigenetic regulation, and proteasomal degradation (Hart, 2014; Bond and Hanover, 2015). Given the diverse roles of *O*-GlcNAcylation, a potential link between hyper-*O*-GlcNAcylation and cancer progression has been proposed (Slawson and Hart, 2011).

Recent evidence has indicated a central role of the HBP in cancer metabolic rewiring and a close association of cancer development with enhanced HBP flux (Chiaradonna *et al*., 2018). Elevated HBP enzyme expression has been detected in multiple human cancers. Itkonen *et al*. reported that UDP-*N*-acetylglucosamine pyrophosphorylase 1 (UAP1), the last enzyme in the pathway, was highly expressed in prostate cancer (Itkonen *et al*., 2015). Oikari *et al.* also described the up-regulation of GFAT, a rate-limiting enzyme of the HBP, in human breast cancer biopsies (Oikari *et al*., 2018), whereby elevated GFAT expression was in parallel with an increase in UDP-GlcNAc content and was strongly correlated with tumor hyaluronan (HA) levels.

HA is a simple glycosaminoglycan in the extracellular matrix (ECM) whose biosynthesis is regulated by three HA synthases (HAS1–3) that link UDP-GlcNAc and UDP-glucuronic acid (UDP-GlcUA) substrates (Toole, 2004) (Figure 3). There is considerable evidence correlating the degree of HA accumulation with a poor prognosis in advanced cancer patients (Anttila *et al*., 2000; Auvinen *et al*., 2000; Heldin *et al*., 2018). Clinicopathological studies have shown high HA levels in the tumor stroma of ovarian and breast cancers to be strongly linked to worse overall and disease-free survival and more frequently observed in metastatic lesions than in primary tumors (Ropponen *et al*., 1998). Our animal studies have furthermore demonstrated that transgenic mice exhibiting HA overproduction in mammary tumors rapidly developed aggressive breast carcinomas, in which plastic cancer cells reverted to stem-cell states (Koyama *et al*., 2007; Koyama *et al*., 2008; Kobayashi *et al*., 2010; Chanmee *et al*., 2014).

HBP flux appears to influence cancer development and progression by controlling UDP-GlcNAc dynamics. However, the mechanisms underlying the cancer pathogenesis associated with enhanced HBP flux have not been fully elucidated. This study investigates the roles of the HBP and its downstream signals in breast cancer to uncover that enhanced

HBP exacerbates cancer by driving metabolic and signaling networks involved in HA production and *O*-GlcNAcylation.

Materials and methods

1. Chemicals and reagents

The following cell culture reagents were used: Dulbecco's modified Eagle's medium (DMEM) (Nacalai Tesque, Osaka, Japan), fetal bovine serum (FBS) (Biosera, Nuaille, France), penicillin-streptomycin (Wako Pure Chemical Industries, Osaka, Japan), glucose-free DMEM (Sigma-Aldrich, St. Louis, MO), DMEM/Ham's F12 (Nacalai Tesque), basic fibroblast growth factor (bFGF) (Wako Pure Chemical Industries, Osaka, Japan), epidermal growth factor (EGF) (Miltenyi Biotec, Bergisch Gladbach, Germany), and B27 (Gibco Life Technologies, Grand Island, NY, USA). The inhibitor DON (6-diazo-5-oxo-L-norleucine) was purchased from Sigma-Aldrich and ST045849 was from TimTec LLC (Newark, DE). The following antibodies were used: anti-*O*-GlcNAc (CTD110.6), anti-OGT (D1D8Q), anti-phospho-Akt (Thr308) (C31E5E), anti-phospho-Akt (Ser473) (D9E), anti-Akt, anti-phospho-Glycogen synthase kinase (GSK) 3β (Ser9), anti-GSK3β (27C10), anti-β-catenin (D10A8), anti-glyceraldehyde-3-phosphate dehydrogenase (GAPDH) (14C10), horseradish peroxidase (HRP)-conjugated anti-mouse IgG, and HRP-conjugated anti-rabbit IgG were purchased from Cell Signaling Technology (Danvers, MA). Anti-β-actin was purchased from Wako Pure Chemical Industries. Anti-GFAT1 and anti-OGA were purchased from Proteintech (Rosemont. IL). The phycoerythrin (PE)-conjugated anti-CD44 and fluorescein isothiocyanate (FITC)-conjugated anti-CD24 antibodies, biotin-conjugated anti-CD31 antibody (RA3-6B2), and biotin-conjugated anti-Ter119 antibody (TER-119) were purchased from eBioscience (San Diego, CA). The PE/Cy7-conjugated anti-Epithelial cell adhesion molecule (EpCAM) antibody was purchased from Biolegend (San Diego, CA). Streptavidin-

Alexa 488 was purchased from ThermoFisher Scientific (Waltham, MA). The sugar nucleotide standards guanosine diphosphoglucose (GDP)-Glucose and UDP-Glucose were purchased from Sigma and UDP-GlcNAc and UDP-GlcUA were purchased from Wako.

2. Microarray

The expression patterns of HBP genes including GFAT, glucosamine-phosphate *N*-acetyltransferase 1 (GNPNAT1), phosphoglucomutase 3 (PGM3), UAP1 and *O*-GlcNAc cycling enzymes including OGT and OGA in breast cancer were estimated using the breast cancer datasets in Oncomine Cancer Microarray database (https://www.oncomine.org). Briefly, target genes were queried in the database and the results were filtered by selecting "breast cancer" and "cancer vs. normal". Statistical comparisons were conducted using Oncomine algorithms. *P*-values less than 0.05 were considered statistically significant. Details of the standardized normalization technique and statistical calculations are available on the Oncomine website.

3. The cBioPortal for the Cancer Genome Atlas analysis

To investigate the genetic status of *HAS2* genes, breast cancer datasets from Molecular Taxonomy of Breast Cancer International Consortium (METABRIC) (2,509 samples) (Pereira *et al*., 2016), Mutational profiles of metastatic breast cancer (France, 2016; 216 samples) (Lefebvre *et al*., 2016), Metastatic Breast Cancer Project (Provisional, April 2018; 157 samples) (http://tcga-data.nci.nih.gov/tcga/), Breast Invasive Carcinoma (TCGA, PanCancer Atlas; 1,084 samples) (Ellrott *et al*., 2018; Gao *et al*., 2018; Hoadley *et al*., 2018; Liu *et al*., 2018; Sanchez-Vega *et al*., 2018; Taylor *et al*., 2018), and Breast Invasive Carcinoma (TCGA, Provisional; 1,105 samples) (https://www.mbcproject.org) were downloaded through the cBioportal web-based utility (http://www.cbioportal.org). The cBioPortal was used to explore the genetic alterations and gene expression across the datasets

(Cerami *et al*., 2012). Raw data of GFAT and HAS2 mRNA expression and clinical information from the METABRIC dataset (EGAS00001001753 from the European Genome-phenome Archive) were employed to evaluate the co-expression of these genes and mRNA expression Z-score associations with clinicopathological characteristics. The correlation between the gene expression of GFAT and/or HAS2 and the overall survival of breast cancer patients was also analyzed by EZR on R commander (Kanda, 2013) using the METABRIC array datasets with 148 cancer samples overexpressing either or both genes. The log rank *p*-value and hazard ratio with 95% confidence intervals were calculated as well.

4. Preparation of primary mouse mammary epithelial cell

Normal mouse mammary epithelial cells (MECs) were isolated as described by Prater *et al*. with some modifications (Prater *et al*., 2013). Mammary glands (No. 3, 4, and 5 gland pairs) were dissected from 13–16-week-old FVB/NJcl mice (CLEA Japan Inc. Tokyo, Japan). The finely minced glands were digested in complete medium (DMEM/F12 containing 5% FBS, 5 μg/ml insulin, 5 ng/ml EGF, 1 μg/ml hydrocortisone, 50 μg/ml gentamycin, 100 U/ml penicillin, and 100 μg/ml streptomycin) containing 1 mg/ml collagenase (Wako Pure Chemical Industries) and 100 U/ml hyaluronidase (Nacalai Tesque) for 16 h at 37 °C. The mammary organoids were digested with 0.25% trypsin (Wako Pure Chemical Industries) and 1 mM Ethylenediaminetetraacetic acid (EDTA) in Hanks's balanced salt solution (HBSS) (Wako Pure Chemical Industries), 5 U/ml dispase (Wako Pure Chemical Industries) in HBSS, and 1 mg/ml DNaseI (StemCell Technologies, Vancouver, Canada) followed by the lysis of red blood cells in NH_4Cl. The single cell suspensions were collected with a 40 μm cell strainer (Corning, Steuben County, NY) and incubated in complete medium for 1 h at 37 °C. After blocking with 10% normal rat serum (Wako Pure Chemical Industries) in DMEM/F12, the mammary cells were stained with anti-CD31-biotin antibody (1:250 dilution) and anti-Ter119-biotin antibody (1:250 dilution) in phosphate buffer saline (PBS) containing 3%

bovine serum albumin (BSA) for 1 h at 4 °C. The cells were then stained with streptavidin-Alexa 488 (1:200 dilution) and anti-EpCAM-PE/Cy7 (1:500 dilution) for 1 h at 4 °C. Cells were sorted using FACSMelody (BD Biosciences, Franklin Lakes, NJ) following filtration through a 42 μm nylon mesh. The high EpCAM-, low CD31-, low TER-119-expressing population was sorted as primary MECs. Total RNA or protein was immediately isolated from sorted MECs using an RNeasy mini kit (Qiagen, Germantown, MD) or radioimmunoprecipitation assay (RIPA) buffer (Nacalai Tesque), respectively. For quantification of HA synthesis, a fraction of the sorted cells was cultured in 96-well plates coated with Matrigel (Wako Pure Chemical Industries).

5. Primary breast carcinoma cells and cell culture conditions

All primary breast carcinoma cells used in this study were established as described previously (Chanmee *et al*., 2014; Chanmee *et al*., 2016). Briefly, $Has2^{flox/flox}$ mice were generated and backcrossed to FVB/N-Tg(MMTV-PyVT)634Mul/J mice. $Has2^{flox/flox}$ breast carcinoma cells were established from primary mammary tumors that had developed spontaneously in $Has2^{flox/flox}$ tumor model mice. $Has2^{flox/flox}$ breast carcinoma cells were infected with the AxCANCre adenovirus carrying the Cre recombinase gene driven by a CAG promoter to generate Has2-deficient $Has2^{\Delta/\Delta}$ cells. $Has2^{flox/flox}$ cells infected with the AxCANLacZ adenovirus carrying the β-galactosidase (LacZ) gene served as a control ($Has2^{flox/flox}$ cells) (Figure 4). All cancer cells were grown in DMEM containing 10% FBS under the standard culture conditions of a humidified atmosphere of 95% air and 5% CO_2 at 37 °C. For the detection of phospho-Akt and GSK3β, $Has2^{flox/flox}$ and $Has2^{\Delta/\Delta}$ cancer cells were grown for 48 h in cell culture medium supplemented with 10% dialyzed FBS and 5.5 mM D-glucose.

6. Quantitative RT-PCR (qRT-PCR)

Total RNA from breast carcinoma cells was isolated using the Qiagen RNeasy mini kit (Qiagen, Germantown, MD). Complementary DNA was synthesized with the PrimeScript RT Reagent kit (Takara Bio, Shiga, Japan) according to the manufacturer's instructions. For murine Has2 and GAPDH, qRT-PCR was performed as described previously (Koyama *et al*., 2007). The TaqMan gene expression assays (Applied Biosystems, Foster City, CA, USA) were as follows: Assay ID: Mm01183874_m1 (GFAT1), Mm00496565_m1 (GFAT2), Mm00834602_mH (GNPNAT1), Mm01144498_m1 (PGM3), Mm01281909_m1 (UAP1), Mm00507317_m1 (OGT), and Mm00452409_m1 (OGA). The RT-PCR conditions for gene expression were as follows: 1 cycle at 94 °C for 30 s and 40 cycles at 94 °C for 3 s and 60 °C for 25 s. Relative mRNA expression was analyzed by the comparative cycle threshold (Ct) method and normalized using GAPDH expression.

7. Gene silencing with short hairpin RNA (shRNA)

Recombinant lentivirus particles were produced by Lenti-vpak lentivirus packaging kit (OriGene, Rockville, MD) with Lenti-X 293T cell (Takara Bio, Kusatsu, Shiga, Japan) according to the manufacturer's instruction. Lentivirus carrying the shRNA of murine GFAT1 (Gene ID 14583, OriGene) and control non-targeting shRNA were infected to $Has2^{flox/flox}$ cells as described previously (Chanmee *et al*., 2016). Transduced cells were then selected in the presence of 10 μg/ml puromycin and 50 μM D-Glucosamine for 14 days. To delete *Has2* gene, shGFAT and shControl cells were infected with AxCANCre and AxCANLacZ adenovirus, respectively, as described previously (Chanmee *et al*., 2016).

8. Determination of HA concentrations by competitive ELISA-like assay

The HA contents of the conditioned medium in exponentially growing cultures were measured by a modified competitive enzyme-linked immunosorbent assay (ELISA) (Koyama

et al., 2007). Briefly, breast cancer cells were cultured for 2 days and the conditioned medium was recovered. The conditioned medium was also recovered from MMTV-PyVT carcinoma cells incubated with or without 20 μM DON (GFAT inhibitor). A mixture of conditioned medium and the biotinylated HA-binding region of aggrecan (b-HABP, Seikagaku Corp. Tokyo, Japan) was added to 96-well plates pre-coated with HA-BSA and then incubated for 1 h at 37 °C. HRP conjugated streptavidin was used as secondary probe, and the enzymatic activity was measured using *o*-phenylenediamine dihydrochloride (Sigma) as a substrate. The HA contents were calculated from a standard curve obtained using serial dilutions of standard HA. HA amounts were normalized with cell number which was determined using cell counting Kit-8 assay (Dojindo Laboratories Co., Kumamoto, Japan).

9. HAS assay

HAS activity was monitored in the cell-free HA synthesis system using UDP-[^{14}C] GlcUA and UDP-GlcNAc as donors and a membrane-rich fraction of the cells as an enzyme source as described previously (Itano *et al*., 1999; Ontong *et al*., 2014). Briefly, the crude membrane fractions isolated from mammary epithelial cells and breast cancer cells were resuspended and incubated at 37 °C for 1 h in 0.2 ml of 25 mM Hepes-NaOH, pH 7.1, 5 mM dithiothreitol, 15 mM $MgCl_2$, 0.1 mM UDP-GlcNAc (Sigma), 2 μM UDP-GlcUA (Nakalai Tesque, Kyoto, Japan) and 2 μCi of UDP-[^{14}C]GlcUA (249 mCi/mmol, PerkinElmer, Boston, MA). Reactions were terminated by adding SDS at 2% (w/v). The incorporation of radioactivity into high molecular mass HA was measured by descending paper chromatography using Whatman No. 3MM paper developed in 1 M ammonium acetate, pH 5.5, and ethanol (65:35). The amounts of radioactivity at the origins were measured by liquid scintillation counting. The HAS activity was determined by calculating the amounts of GlcUA incorporated using known specific radioactivities.

10. UDP-sugar quantification by High-performance liquid chromatography (HPLC)

UDP-sugars were quantified by Ion-pair reverse-phase HPLC methods as described by Nakajima *et al*. with some modifications (Nakajima *et al*., 2010). Cellular extracts were prepared from 300,000 to 500,000 of each cell. Cells were washed twice with cold PBS, immediately snap-frozen the plate with liquid nitrogen, scraped off three times with 500 µl of 70% ice-cold ethanol (total 1.5 ml) and finally the whole cell lysates were snap-frozen in liquid nitrogen. Cell suspensions were sonicated following centrifugation at 16,000 g for 15 min at 4 ^{o}C to remove an insoluble material. The supernatant was collected and evaporated using a lyophilizer. The freeze-dried samples were subjected to ion-pair solid-phase extraction using an Envi-Carb column (Supelco Inc, Bellefonte, PA). The column was activated with 1 ml of 80% acetonitrile in 0.1% trifluoroacetic acid followed by washing with 2 ml of water. Samples were dissolved in 10 mM NH_4HCO_3 and spiked with the unnatural nucleotide sugar, GDP-Glc (500 pmol), which was used as an internal standard to normalize the recovery in sample preparation. After that sample was transferred into column, followed by washing with water, 25% acetonitrile, water and 50 mM triethylamine acetate buffer (pH 7), respectively. Binding nucleotide sugars were eluted with 25% acetonitrile in 50 mM triethylamine acetate buffer (pH 7). Finally, the samples were lyophilized and stored at −80°C until analyzed. The UDP-sugars were quantified by HPLC system (Shimazu, Kyoto, Japan) using an Inertsil ODS-3 column (250 × 4.6 mm internal diameter, 3 µm particle size; GL Science, Tokyo, Japan). The column temperature was set at 40 °C. For HPLC analysis, the mobile phase buffer A (100 mM potassium phosphate buffer pH 6.4 contained 8 mM tetrabutylammonium hydrogensulphate) and buffer B (70% buffer A with 30% acetonitrile) were used. All buffers were filtered on 0.45µm filters (Millicup) under vacuum and degassed in a Bioraptor Sonicator before using. After equilibration a column with 100% buffer A, the 20 µl of sample (dissolved in water) was injected. The gradient elution was performed by

100% buffer A for 35 min; 0-77% linear gradient of buffer B for 40 min; 77-100% buffer B for 1 min and 100% buffer B for 24 min at a flow rate of 0.8 ml/min. Nucleotide sugars were analyzed with UV detection at 254 nm. Concentration of nucleotide sugars in samples were quantified from the linear regression of standards curve and reported as pmole/10^3 cells unit.

11. Sodium dodecyl sulphate-polyacrylamide gel electrophoresis (SDS-PAGE) and Western Blot

SDS-PAGE and western blotting were performed as described previously (Chanmee *et al*., 2016). Breast cancer cells were seeded at 2.5 × 10^5 cells/well and cultured in 10% FBS/DMEM with or without 50 µM ST045849 or 20 µM DON for 3–48 h. Cells were harvested at indicated times, washed with cold PBS, and lysed in RIPA buffer (50 mM Tris-HCl, pH 7.6, 150 mM NaCl, 1% Nonidet P40, 0.5% sodium deoxycholate, 1X protease inhibitor cocktail [EDTA free], and 0.1% SDS) (Nacalai Tesque). For detection of phosphorylated proteins, cells were lysed in RIPA buffer containing phosphatase inhibitor cocktail (Nacalai Tesque). Protein concentrations were determined by the Pierce Microplate BCA protein assay kit (Thermo Scientific) according to the manufacturer's instructions. Equal amounts of whole cell lysates (2 µg) were subjected to SDS-PAGE on 8%-12% polyacrylamide gels. After protein transfer to polyvinylidene fluoride (PVDF) membranes (Millipore, Burlington, MA), the membranes were blocked with 0.1% Tween in tris-buffered saline (TBS) (50 mM Tris-HCl, pH 7.4, 138 mM NaCl, 2.7 mM KCl, and 0.1% Tween 20) containing 5% BSA (Nacalai Tesque) or 5% skim milk for 60 min at room temperature on a shaker. The membranes were then probed with the primary antibody anti-*O*-GlcNAc (1:1000 dilution), anti-GFAT1 (1:1000 dilution), anti-OGT (1:1000 dilution), anti-OGA (1:3000 dilution), anti-p-Akt Ser473 (1:2000 dilution), anti-p-Akt Thr 308 (1:1000 dilution), anti-p-GSK3β Ser9 (1:1000 dilution), anti-β-catenin (1:2000 dilution), anti-Akt (1:1000 dilution), or anti-GSK3β (1:1000 dilution) at 4 °C overnight. Anti-β-actin antibody or anti-GAPDH

antibody was used as an internal control. Excess antibodies were removed by washing in 0.1% Tween-TBS, with subsequent incubation with HRP-conjugated secondary antibodies (1:2000 dilution) for 60 min at room temperature. Signals were visualized using western blotting detection reagents (Wako Pure Chemical Industries). Chemiluminescent signals were observed on an ImageQuant LAS4000 Mini Luminescent image analyzer (GE Healthcare, Chicago, IL). Band intensities were quantified by densitometric analysis using ImageJ software (National Institutes of Health, Bethesda, MD).

12. Apoptosis analysis

One hundred thousand of $Has2^{flox/flox}$ and $Has2^{\Delta/\Delta}$ cells were cultured in 35 mm dish for 24 h and then treated with 0 – 50 μM cisplatin (Wako Pure Chemical Industries, Osaka, Japan) alone or combination with 50 μM ST045849 in DMEM containing 10% FBS. After incubation for 16 h, total cells were harvested by collecting the all media, washing with PBS, trypsinization, and centrifugation at 1,200 g for 5 min. Cells were then suspended in 10% FBS/DMEM. Apoptotic cells were analyzed using MEBCYTO Apoptosis Kit (MBL Co., Ltd., Nagoya, Japan). The cells at 2 x 10^5 cells were resuspended in 85 μl binding buffer solution containing 7 μl of Annexin V-FITC and 5 μl of propidium iodide (PI). Cells were then incubated at room temperature in dark place for 15 min. The 400 μl of binding buffer solution were added to each tube and mixed gently by pipetting. The cells were filtrated through cell strainers with a 48-μm nylon mesh (N-No3305T: NBC Meshtec, Tokyo, Japan) and then analyzed by FACSCalibur (BD Biosciences, Franklin Lakes, NJ).

13. $CD44^{high}/CD24^{low}$ cell population by flow cytometric analysis

Breast carcinoma cells were seeded at 1 × 10^5 cells/35 mm dish and cultured at 37 °C for 24 h in DMEM containing 10% FBS. For inhibitor experiments, cancer cells were treated with or without 50 μM ST045849 or 20 μM DON every 3 days and incubated for 7 days.

Then, 5×10^5 cells were harvested and washed in cold PBS supplemented with 1% FBS. Cell suspensions were incubated with 50 µl of 1% FBS-PBS containing PE-conjugated anti-CD44 (1:160 dilution) and FITC-conjugated anti-CD24 (1:50 dilution) or PE-Cy-5-conjugated anti-CD24 antibodies (1:800 dilution) antibodies for 60 min on ice in dark place. The cells were washed with FBS by centrifugation, discarded supernatant and then resuspened in cold 1% FBS/PBS following filtered through cell strainers with a 48-µm nylon mesh. A total of 10,000 viable cells were analyzed using the FACSMelody cell sorter (BD Biosciences) (Chanmee *et al*., 2016).

14. Mammosphere formation assay

The mammosphere formation assay was performed as described previously (Chanmee *et al*., 2014). The breast carcinoma cells were plated into ultralow attachment 24-well plates (Corning) at a density of 5,000 cells and grown in serum-free DMEM/Ham's F12 supplemented with 20 ng/ml bFGF, 20 ng/ml EGF, and 1X B27. Fresh medium of 500 µl was replenished every 3 days during continuous culture for 7 days. The number of spheres greater than 75 µm in diameter was counted under a phase-contrast microscope. For inhibitor treatments, breast carcinoma cells were cultured in medium with or without the 50 µM ST045849 or 20 µM DON inhibitors for 7 days.

15. Aldehyde dehydrogenase (ALDH) activity by flow cytrometric analysis

ALDH activity was measured using flow cytometry analysis. The ALDEFLUOR Kit (Stem Cell Technologies, Vancouver, Canada) was used to measure cell populations with high ALDH activity, according to the manufacturer's instructions. Briefly, the breast cancer cells (4×10^5 cells) were collected and centrifuged at 1,200 g for 5 min. The supernatant was discarded and resuspened with 400 µl of ALDEFLUOR™ assay buffer. The 4 µl of 3 µM BODIPY-aminoacetaldehyde was added to the sample and mixed by pipetting (labelled as

test tube). The 200 µl aliquot of a sample mixture was immediately transferred to new tube and incubated with the 2 µl of 15 µM diethylaminobenzaldehyde (DEAB), which is a specific ALDH inhibitor (labelled as control tube). All samples were incubated at 37 °C for 60 min in dark place. After that all tubes were centrifuged at 2,500 g for 5 min and removed supernatant. The cell pellets were resuspended with 300 µl of ALDEFLUOR™ assay buffer and followed by filtration through a 48-µm nylon mesh. The ALDEFLUOR-positive cells were analyzed and control tube of each samples were used to set a baseline and defined the cut-off threshold for ALDEFLUOR-positive cells. A total of 20,000 viable cells were analyzed using the FACSMelody cell sorter (BD Biosciences).

16. Tumorigenicity assay

The control $Has2^{flox/flox}$ and Has2-deficient $Has2^{\Delta/\Delta}$ cells (1×10^6 cells/injection) were suspended in HBSS and injected subcutaneously into BALB/c nude mice (n = 6 per group, CLEA Japan, Inc., Tokyo, Japan). Tumor size was recorded for 35 days after inoculation. Tumor diameter was measured every 2 to 4 days with digital calipers. The tumor volume was calculated by the formula: volume = $(\text{width})^2 \times \text{length}/2$. Animal care and all experimental procedures using animal models were performed in biosafety level 2 animal facilities according to the established guidelines approved by the Kyoto Sangyo University ethics committee.

17. Statistical analysis

The two-tailed Student's t-test or Tukey's multiple comparison test was used to determine the differences among means. Data were expressed as the mean ± standard deviation (S.D.) A *p*-value of less than 0.05 was considered statistically significant.

Results

1. Up-regulation of HBP-related genes in clinical breast cancer

Oncomine microarray gene expression datasets were initially analyzed across different types of clinical breast cancers for the expression of genes encoding HBP enzymes, including GFAT, GNPNAT1, PGM3, and UAP1, to investigate the molecular mechanisms underlying cancer pathogenesis associated with enhanced HBP flux (Rhodes *et al*., 2004; Rhodes *et al*., 2007). The Ma Breast 4 dataset displayed significantly higher expression of all HBP genes in ductal breast carcinoma *in situ* epithelia (n = 9) than in normal samples (n = 14) (Figure 5 and Table 1) Databases were further searched for the expression of HBP enzymes across several datasets (Table 1). Eight of 11 datasets showed that the expression of GFAT (GFAT1/2) was elevated over 1.5-fold in various types of breast cancers compared with normal samples. GFAT expression was often up-regulated together with GNPNAT1 and UAP1. In some datasets where GFAT expression was not significantly increased, one of GNPNAT1, PGM3, or UAP1 was highly expressed in cancer tissues. Thus, *in silico* gene expression analysis suggested the up-regulation of essential HBP enzymes in breast cancers across datasets.

2. Co-expression of GFAT and HAS2 in aggressive breast cancers

Since the significance of HA in tumor development has been highlighted by several pathological and experimental studies, I focused on this polysaccharide and its metabolism that is dynamically regulated by HBP flux. The genetic status of the three *HAS* genes was investigated in The Cancer Genome Atlas breast cancer database using cBioPortal (http://www.cbioportal.org/), which revealed that *HAS2* amplification was significantly higher in breast cancer across 5 datasets (Figure 6A). I next addressed the association between *HAS2* amplification and overall survival in breast cancer patients. Kaplan–Meier analysis of 5071 patients demonstrated that *HAS2* amplification was significantly correlated

with shorter overall survival (Figure 6B). To further identify relationships between histological subtypes and genetic alterations, samples in TCGA PanCancer Atlas dataset comprising 1070 patient cases were evaluated (Weinstein *et al*., 2013). *HAS2* was amplified in 13% of all breast cancers and 25% of metaplastic breast cancers, the latter being rare and aggressive variants (Figure 6C). In accordance with the gene amplification results, *HAS2* was transcriptionally active in aggressive metaplastic breast cancer (Figure 6D). Relationships between *HAS2* expression patterns and patient clinicopathological attributes were then examined using Molecular Taxonomy of Breast Cancer International Consortium datasets (n = 2509, Figure 7A) (Curtis *et al*., 2012; Pereira *et al*., 2016). Gene expression profiling suggested a significant correlation ($r = 0.4$, $p < 0.05$) between GFAT (GFAT1/2) and HAS2 expression (Figure 7A and 7B). Kaplan–Meier survival analysis of breast cancer patients (n = 148) demonstrated co-expression of GFAT and HAS2 to be more significantly associated with worse overall patient survival than the respective expression of GFAT or HAS2 alone (Figure 7C). Multidimensional data analysis therefore indicated that co-expression of GFAT and HAS2 predicted a poor outcome.

Gene expression patterns were further assessed using METABRIC datasets of intrinsic molecular subtypes of breast cancer (luminal A, luminal B, normal breast-like, HER2-enriched, claudin-low, and basal-like). Of note, HAS2 positivity was enriched in basal-like and claudin-low subtypes, which became more prominent in combination with GFAT positivity (Figure 8). Considering that the basal-like and claudin-low subtypes belong to the group of triple-negative breast cancer having a high incidence of recurrence and metastasis, the co-expression of GFAT and HAS2 may confer aggressiveness in human breast cancer.

3. Elevated expression of HBP gene, hyper O-GlcNAcylation, and increased HA production in a mouse model of aggressive breast cancer

I next sought to validate the findings from human clinical samples using murine breast cancer models. Mouse mammary tumor virus (MMTV)-Neu and mouse mammary tumor virus promoter-driven polyoma middle T (MMTV-PyVT) transgenic (Tg) mice were employed as murine breast cancer models for measuring the gene expression of HBP enzymes (Guy *et al*., 1992a; Guy *et al*., 1992b). Both Tg lines develop palpable mammary tumors, while the MMTV-Neu phenotype differs from that of the MMTV-PyVT line recapitulating the progression of human mammary adenoma to late carcinoma stages and metastasizing primarily to the lymph nodes. Primary breast carcinoma cells were established from mammary tumors that had developed spontaneously in the MMTV-Neu and MMTV-PyVT mice and subjected to qRT-PCR analysis of HBP enzyme expression levels. The mRNA expression of GFAT1, GNPNAT1, PGM3, and UAP1 was significantly elevated in both primary carcinoma cell sets, particularly in the aggressive carcinoma cells derived from MMTV-PyVT tumors, as compared with the mammary epithelial cells of control mice (Table 2), which was in fair agreement with the Oncomine database analysis. Significantly increased expression of GFAT1 mRNA was seen in MMTV-PyVT carcinoma cells, while GFAT2 mRNA expression in MMTV-Neu and MMTV-PyVT cells was markedly less than in controls (Table 2). The increased expression of GFAT1 was validated at the protein level by western blot analysis (Figure 9A), implying that the HBP was closely associated with breast cancer aggressiveness. To determine if the elevated expression of HBP enzymes increased the cellular pool of UDP-GlcNAc, UDP-sugars were monitored using HPLC. The cellular levels of UDP-GlcNAc as well as UDP-Glucose (UDP-Glc) and UDP-GlcUA were significantly increased in MMTV-PyVT carcinoma cells as compared with MECs and MMTV-Neu cells (Figure 10).

The elevated expression of HBP enzymes and enhanced HBP flux may increase levels of protein *O*-GlcNAcylation and HA production by supplying additional UDP-GlcNAc. To ascertain this possibility, I examined the *O*-GlcNAc status of proteins by western blot analysis using anti-*O*-GlcNAc antibodies. Overall protein *O*-GlcNAcylation was significantly elevated in both malignant carcinoma cell lines as compared with MECs (Figure 11A). It was noteworthy that the highest level of *O*-GlcNAcylation was detected in MMTV-PyVT cancer cells, which corroborated the increased level of UDP-GlcNAc. *O*-GlcNAc cycling enzyme expression was assessed by western blot analysis. In comparison with MECs, OGT expression was significantly down-regulated in both primary carcinoma cell lines (Figure 9B). Given that cellular UDP-GlcNAc was significantly higher in these cancer cells than MECs (Figure 10), it is plausible that the levels of protein *O*-GlcNAcylation is predominantly controlled by HBP flux rather than OGT expression in these cells. In fact, a competitive GFAT antagonist, DON decreased *O*-GlcNAc level in MMTV-PyVT cancer cells (Figure 12A), suggesting a crucial role of HBP flux in the determination of protein *O*-GlcNAcylation. The OGA expression was down-regulated in MMTV-PyVT cancer cells (Figure 9C), which was inversely correlated with the highest level of *O*-GlcNAcylation. The low OGA expression in MMTV-PyVT cells was consistent with the Oncomine meta-analysis of breast cancer microarray database (Table 3). On the other hand, the OGA expression in MMTV-Neu cancer cells was higher than that in MMTV-PyVT cells (Figure 9C). The observations therefore imply that the OGA expression might be associated with the levels of protein *O*-GlcNAcylation.

When HA production was examined by a competitive ELISA-like assay, it was seen to be increased in MMTV-PyVT cancer cells but not in MMTV-Neu cells (Figure 11B). Consistently with HA production level, *Has2* gene expression and HAS activity were elevated over 4-fold ($p < 0.05$) in MMTV-PyVT carcinoma cells (Figure 11C and 11D),

which strengthened the above notion that the coordinated up-regulation of both GFAT and HAS2 expression might confer aggressiveness in human breast cancer. Although gene expression profiles and HAS activity suggested that the up-regulation of Has2 was primarily responsible for the higher HA production in MMTV-PyVT cancer cells, enhanced HBP flux was also suspected to augment in the production of HA as HA level was decreased by DON exposure and rescued by D-Glucosamine (GlcN) (Figure 12B).

4. HA production promotes CSC-like features and aggressive tumor growth

To gain a better understanding of HA function in PyVT-induced carcinogenesis, MMTV-PyVT cancer cells harboring homozygous Has2 floxed alleles ($Has2^{flox/flox}$ cells) were compared with Has2-deficient $Has2^{\Delta/\Delta}$ cells (Figure 4). As evidenced by our previous study (Chanmee *et al*., 2016), Cre-mediated recombination of the Has2 locus induced an almost complete failure of Has2 expression and HA production in $Has2^{\Delta/\Delta}$ cells (Figure 13A and 13B). When Has2-deficient $Has2^{\Delta/\Delta}$ cancer cells were then transplanted into the mammary fat pads of nude mice, tumor growth was significantly suppressed as compared with that of the control $Has2^{flox/flox}$ group (Figure 13C). The mean tumor volume of the control $Has2^{flox/flox}$ group reached 1035.8 ± 941.5 mm^3 on day 30 post-tumor cell injection, whereas that of the $Has2^{\Delta/\Delta}$ group was only 155.5 ± 17.0 mm^3. These data highlighted the significance of HA in cancer growth.

CSCs are believed to drive cancer growth and progression through aberrant self-renewal and the generation of heterogeneous cancer cell lineages (Chanmee *et al*., 2015). CSC-like cells were assessed for the expression of CD44 and CD24 by flow cytometric analysis before and after deletion of the *Has2* gene. Has2-deficient $Has2^{\Delta/\Delta}$ cancer cells exhibited a markedly reduced $CD44^{high}/CD24^{low}$ CSC-like subpopulation as compared with control $Has2^{flox/flox}$ cancer cells (Figure 14A). Aldehyde dehydrogenase-positive ($ALDH^+$) populations from multiple types of cancers have been demonstrated to be enriched in cancer

cells with stem-like characteristics and tumor-initiating ability (Ma and Allan, 2011; Xu *et al*., 2015). In Aldefluor flow cytometry assays, $Has2^{\Delta/\Delta}$ cancer cells displayed a smaller $ALDH^{+}$ cell population than did control $Has2^{flox/flox}$ cancer cells (Figure 14B). Breast CSCs have also been reported to form floating spherical colonies termed mammospheres to survive and proliferate in anchorage-independent conditions (Grimshaw *et al*., 2008). Control $Has2^{flox/flox}$ cancer cells were capable of forming large mammospheres with high efficiency, whereas Has2-deficient $Has2^{\Delta/\Delta}$ cancer cells mainly formed small mammospheres of 75-150 μm in diameter (Figure 15). CSCs often acquire resistance to anticancer drugs and are thereby thought to be responsible for tumor recurrence following treatment. Platinum-based chemotherapeutic drugs such as cisplatin are commonly used for treating metastatic triple-negative or basal-like breast cancers. Has2-deficient $Has2^{\Delta/\Delta}$ and control $Has2^{flox/flox}$ cancer cells were treated with cisplatin and the percentage of early and late apoptotic cells was determined by dual staining with fluorescent Annexin V and PI. Early apoptotic cells showed Annexin V^{+}/PI^{-} staining patterns, while late apoptotic cells exhibited Annexin V^{+}/PI^{+} patterns. After exposure to cisplatin, a significant increase in early and late apoptotic cells was observed in Has2-deficient $Has2^{\Delta/\Delta}$ cells (Figure 16). Taken together, these findings were in agreement with our previous study demonstrating a role of HA production in the regulation of CSC-like features and tumorigenesis.

5. HA triggers the pro-oncogenic Akt/GSK3β/β-catenin signaling pathway

I next aimed to identify the signaling pathways involved in the pro-tumorigenic actions of HA. The phosphatidylinositol-3-kinase (PI3K)/Akt signaling pathway has emerged as a pro-tumorigenic signal, with recent studies showing links to CSC self-renewal (Martelli *et al*., 2010; Janku *et al*., 2018). GSK3β governs several signaling pathways associated with cancer progression and is inactivated upon phosphorylation in an Akt-dependent manner (Luo, 2009). The Has2-deficient $Has2^{\Delta/\Delta}$ cancer cells displayed greatly reduced Akt

phosphorylation at both Serine473 (Ser473) and Threonine308 (Thr308) as well as GSK3β phosphorylation at Serine9 (Ser9) as compared with control $Has2^{flox/flox}$ cells (Figure 17A and 17B). The phosphorylation of GSK3β inhibits its activity and prevents it from phosphorylating β-catenin, thus allowing the stabilization and nuclear translocation of β-catenin (Wu and He, 2006). The stabilized β-catenin subsequently activates target genes by binding to TCF/LET transcription factors and induces the epithelial-mesenchymal transition (EMT) crucial for the maintenance and expansion of CSCs. In accordance with the reduced phosphorylation of GSK3β, the expression of β-catenin was decreased in Has2-deficient $Has2^{\Delta/\Delta}$ cancer cells (Figure 17C).

6. Coordinated actions of GFAT and Has2 on the regulating of CSC-like feature

The multidimensional analysis of the clinical microarray datasets and comparative study of distinct breast cancer mouse models suggested GFAT and HAS2 co-expression in malignant breast cancer, which prompted me to examine whether the coordinated action of these enzymes was crucial for regulating CSC-like features. For this purpose, *GFAT1* gene expression was silenced in $Has2^{flox/flox}$ cancer cells. A shRNA against murine GFAT1 mRNA was introduced into $Has2^{flox/flox}$ cells by means of a lentiviral vector. As a negative control for the experiments, $Has2^{flox/flox}$ cells were infected with control lentivirus composed of non-targeting shRNA. The transduced cells were analyzed for endogenous GFAT1 protein and mRNA levels by western blot analysis and qRT-PCR, respectively (Figure 18A and 18B). GFAT1 knockdown decreased its protein expression by approximately 50% as compared with $Has2^{flox/flox}$ cells with control shRNA. GFAT1 silencing resulted in a moderate reduction in *O*-GlcNAcylation as well (Figure 18C), while the expression levels of OGT and OGA were unaffected by GFAT1 silencing (Figure 19A and 19B). Consistently with the decreased GFAT1 expression, cellular UDP-GlcNAc levels were lowered in the GFAT1 knockdown cells (Figure 18D). Interestingly, GFAT1 knockdown significantly reduced *Has2* gene

expression as well as HA production (Figure 20A and 20B), suggesting GFAT-dependent regulation of Has2 expression. GFAT1 knockdown cells were then analyzed the expression of CD44 and CD24 and ALDH activity by flow cytometric analysis. GFAT1 silencing reduced both $CD44^{high}/CD24^{low}$ CSC-like subpopulation and $ALDH^{+}$ cell population (Figure 21 and Figure 22). Similarly to *Has2* gene deletion, GFAT1 silencing reduced mammosphere size as the number of small mammospheres increased (Figure 23). The pharmacological inhibition of GFAT with DON also markedly reduced $CD44^{high}/CD24^{low}$ subpopulation and mammosphere formation in MMTV-PyVT cancer cells (Figure 24A and 24B). GFAT1 knockdown cells were then analyzed before and after *Has2* gene disruption for the expression of CD44 and CD24 and mammosphere formation. Cre-mediated recombination of the *Has2* gene locus induced an almost complete failure of *Has2* gene expression in the GFAT1 knockdown cells (Figure 20A). Has2 deletion showed more remarkable effects on the attenuation of the $CD44^{high}/CD24^{low}$ CSC-like subpopulation than did GFAT1 knockdown alone. Compared with GFAT1 single knockdown, both the size and number of large mammospheres over 150 μm in diameter were reduced by the combination of GFAT1 knockdown and Has2 knockout (Figure 23). These results suggest the coordinated actions of GFAT1 and Has2 on the regulation of CSC-like phenotypes.

7. HA and O-GlcNAcylation signaling pathways play overlapping but distinct roles in the regulation of CSC-like phenotypes

The HBP serves as a key metabolic pathway essential for signaling networks involving protein *O*-GlcNAcylation. Hence, I investigated whether protein *O*-GlcNAcylation regulated CSC-like features as a HBP downstream signal. When the selective OGT inhibitor ST045849 was applied to MMTV-PyVT cancer cells ordinarily exhibiting hyper-*O*-GlcNAcylation, the overall levels of protein *O*-GlcNAcylation became significantly attenuated compared with the untreated control group (Figure 25). Consistently with the

reduced *O*-GlcNAcylation, pharmacological inhibition greatly diminished the $CD44^{high}/CD24^{low}$ CSC-like subpopulation and the number of mammospheres (Figure 26A and 26B). Moreover, OGT inhibition strengthened the suppressive effect of a Has2 deficiency (Figure 28A and 28B). In contrast, the $ALDH^{+}$ cell population was scarcely affected by OGT inhibitor treatment (Figure 27). The above results therefore indicate that HBP flux comprehensively regulates CSC-like features by driving HA and *O*-GlcNAcylation signaling pathways.

A synergistic effect of cisplatin and an OGT inhibitor was then evaluated by Annexin V apoptosis assay. The rate of apoptotic cells was unchanged after exposure to cisplatin despite co-treatment with OGT inhibitor (Figure 29). Surprisingly, the OGT inhibition almost completely rescued cisplatin resistance that had been suppressed by Has2 deficiency (Figure 29), implying that the hypo-*O*-GlcNAcylation may abolish the therapeutic efficacy of HA signal blockade against cisplatin resistance.

Discussion

The HBP has emerged as a nutrient sensor that integrates nutrient availability with numerous cellular signaling pathways. The present study provided several lines of evidence that enhanced HBP flux drove metabolic and signaling networks involving HA and *O*-GlcNAcylation in aggressive breast cancer: (1) essential enzymes in the HBP were up-regulated in breast cancer cells, which was in agreement with findings in human clinical samples; (2) the *HAS2* gene was amplified in human breast cancers, and the expression of this gene was associated with aggressive types of breast cancer; (3) co-expression of HAS2 and GFAT was correlated with poor prognosis in advanced breast cancer patients and cancer cell aggressiveness; (4) GFAT suppression diminished CSC-like features along with the reduction of HA production and protein *O*-GlcNAcylation; (5) gene targeting of Has2 significantly suppressed CSC-like phenotypes and xenograft tumor growth and attenuated the pro-tumorigenic Akt/GSK3β/β-catenin signal and anti-cancer drug resistance; (6) HA and *O*-GlcNAcylation signaling pathways play overlapping but distinct roles in the regulation of CSC-like phenotypes (Figure 30).

Previous studies have identified that HA accumulation in many cancer tissues and associated increased HA amounts with less favorable outcome (Auvinen *et al*., 2014). In this investigation, *HAS2* gene amplification was augmented in aggressive breast carcinomas in analysis of TCGA datasets for cancer genomics, thus supporting the importance of this genetic event in breast cancer development and progression. Such an amplification may reflect the up-regulation of *HAS2* expression in progressed breast cancer; indeed, the *HAS2* gene expression was frequently up-regulated in aggressive metaplastic breast carcinomas, indicating the importance of HAS2 in aggressive breast cancer. This notion was supported by the fact that Has2 deletion in MMTV-PyVT carcinoma cells significantly suppressed xenograft tumor growth. Considering that HAS2 positivity was highly associated with the

basal-like and claudin-low cancer subtypes enriched with features of EMT, Has2 expression appeared to be closely linked to malignant cancer cells undergoing EMT. In support of this, our previous study demonstrated that forced expression of Has2 in MMTV-Neu mammary tumors allowed plastic cancer cell populations to revert to stem-cell states via the induction of EMT (Chanmee *et al*., 2014).

HA has been shown to provide a favorable microenvironment for the self-renewal and maintenance of CSCs. Bourguignon *et al.* demonstrated that interactions between HA and its receptor, CD44v3, propagated cancer stemness of human head and neck squamous cell carcinoma cells via the stem cell factors Oct4, Sox2, and Nanog (Bourguignon *et al*., 2017). Ohno *et al.* recently reported that HA-CD44 interactions regulated the spheroid formation and maintenance of cancer-initiating cells in malignant mesothelioma (Ohno *et al*., 2018). HA in the tumor microenvironment also indirectly affected CSC self-renewal by influencing the behavior of stromal cells (Okuda *et al*., 2012). In contrast, I have recently found that HA production may metabolically regulate CSC properties (Chanmee *et al*., 2016), although the precise mechanism remains unknown. Since HA is normally synthesized at the plasma membrane using donor substrates, its overproduction can directly reduce cytosolic UDP-GlcUA and UDP-GlcNAc levels. Therefore, HA-overproducing cells may accelerate HBP flux to balance synthesis and consumption of UDP-GlcNAc. This was evident from the fact that forced expression of Has2 in MMTV-Neu cancer cells significantly accelerated HBP flux (Chanmee *et al*., 2016). The HBP senses the reduction of cytosolic UDP-GlcNAc availability and accelerates the rate-limiting step catalyzed by GFAT, thus serving to provide sufficient UDP-GlcNAc (Taparra *et al*., 2016). Therefore, the positive feedback loop between HBP changes and HA production may act in a system amplifying a series of signals triggered by accelerated HBP flux. It will be of interest to further explore whether HA regulates CSC-like features not only by evoking signals in a receptor-mediated fashion, but also by modulating

cellular signaling via its biosynthesis.

The present study indicated that co-expression of HAS2 and GFAT was highly associated with the aggressive cancer subtypes and strongly correlated with a poor prognosis in advanced cancer patients. In agreement with the clinical data, GFAT1 and Has2 co-expression was evident in aggressive MMTV-PyVT cancer cells. The coordinated regulation of *GFAT* and *Has2* gene expression was further supported by the result that GFAT1 knockdown in MMTV-PyVT mammary carcinoma cells significantly reduced *Has2* gene expression. The promoter region of the *HAS2* gene contains functional response elements for several transcription factors, including CREB, STAT3, FOXO1, SP1, and YY1. Dynamic HBP flux regulates the transcriptional activation of these factors through *O*-GlcNAcylation. Jokela *et al*. have demonstrated that GFAT1 silencing in HaCaT keratinocytes increased HAS2 expression by limiting the *O*-GlcNAc-modification of SP1 and YY1 (Jokela *et al*., 2011). The difference in the cellular responsiveness of mammary carcinoma cells and keratinocytes to GFAT silencing may be attributed to the expression patterns of transcriptional regulators in these cells. HAS2-AS1, a natural antisense transcript, has also been reported to regulate HAS2 transcription by altering the chromatin structure around the HAS2 proximal promoter (Vigetti *et al*., 2014). *O*-GlcNAcylation modulates HAS2-AS1 promoter activation by recruiting the NF-κB subunit p65. Therefore, both HBP flux and downstream *O*-GlcNAcylation may multiply regulate HAS2 expression by context-dependent mechanisms via transcription factors and HAS2-AS1.

The suppressive effects of GFAT1 silencing on mammosphere formation resembled those of a Has2 deficiency, which further strengthened the conclusion that GFAT1 and Has2 coordinately regulate CSC-like features. GFAT1 silencing was sufficient to reduce HA production, but only had a moderate effect on suppressing *O*-GlcNAcylation. Given these results, HA signaling may be dominantly affected by changes in HBP flux while cellular *O*-

GlcNAc levels are somewhat maintained within an optimal range. The existence of a feedback loop that maintains *O*-GlcNAc homeostasis has been demonstrated by the fact that the reduction of cellular UDP-GlcNAc level up-regulated OGT expression and down-regulated OGA expression (Cheung and Hart, 2008; Taylor *et al*., 2008). However, this was not the case in our cancer cell system, because the expression levels of OGT and OGA were unaffected by GFAT1 silencing (Figure 19A and 19B). *O*-GlcNAc homeostasis is determined by the availability of donor and acceptor substrates as well as by OGT/OGA expression and activity. Since it is possible that HA biosynthesis and *O*-GlcNAcylation compete for the availability of a donor UDP-GlcNAc substrate, the different kinetics between the enzymes involved in both reactions may be critical for determining which signaling pathway is dominant to control mammosphere formation as a HBP downstream signal. The lowest *Km* of the OGT active subunit is almost 5-fold less than that of Has2, supporting the notion that changes in HBP flux preferentially affect HA signaling over *O*-GlcNAcylation (Itano *et al*., 1999; Kreppel and Hart, 1999).

Mammosphere number and size reflect the self-renewal and proliferation of mammary stem/progenitor cells, respectively (Dontu *et al*., 2003; Dontu *et al*., 2004). I observed that while OGT inhibition markedly reduced the size and number of mammospheres, GFAT1 knockdown or *Has2* gene deletion only reduced their size. OGT inhibition further reduced the number of mammospheres whose size was diminished by a Has2 deficiency. Therefore, I postulate that *O*-GlcNAcylation modulates the key signals necessary for stem cell self-renewal, whereas HA signaling promotes the proliferation of cells with sphere-forming ability. Collectively, enhanced HA and *O*-GlcNAcylation signals may complementarily or synergistically promote CSC-like features as downstream signals of the HBP. Although the mechanism of mammosphere size regulation is currently unclear, the PI3K/Akt survival signal triggered by HA may contribute to the proliferation and viability of stem-like cells in

anchorage-independent conditions (Lawlor *et al*., 2002).

$CD44^{high}/CD24^{low}$ and $ALDH^{high}$ have been widely-accepted as CSC-like phenotypes in breast cancer. To date, however, the relationship between different phenotypes has not been clearly established. In the current study, OGT inhibition altered CD44/CD24 expression, but not ALDH activity; hence, these phenotypes may be regulated in an independent manner. Considering that a Has2 deficiency attenuated ALDH activity as well as the $CD44^{high}/CD24^{low}$ subpopulation, enhanced HA and *O*-GlcNAcylation signals may additively or synergistically promote the $CD44^{high}/CD24^{low}$ CSC-like phenotype.

A Has2 deficiency significantly suppressed the cisplatin resistance that was unaffected by OGT inhibition, suggesting distinct roles between HA and *O*-GlcNAcylation signaling pathways in cisplatin resistance. PI3K/Akt/mTOR pathway activation has been implicated in the cisplatin resistance of triple-negative breast cancer cells (Gohr *et al*., 2017). Considering that a Has2 deficiency attenuated both PI3K/Akt signaling and cisplatin resistance, the HA/PI3K/Akt signaling axis appears to be important for the acquisition of drug resistance. On the other hand, the hypo-*O*-GlcNAcylation induced by OGT inhibition almost completely rescued the cisplatin resistance that had been suppressed by a Has2 deficiency, suggesting that potent inhibition of *O*-GlcNAcylation may abolish the therapeutic efficacy of a HA signal blockade against cisplatin resistance. The contradictory action of *O*-GlcNAcylation on cisplatin resistance may therefore be attributed to aberrant hypo-*O*-GlcNAcylation arising from OGT inhibitor treatment. Hence, the development of CSC therapeutics based on *O*-GlcNAcylation inhibition requires careful consideration.

In conclusion, I uncovered that an enhanced HBP drove pro-tumorigenic signaling pathways involving HA and *O*-GlcNAcylation in aggressive breast cancer. Furthermore, the HA and *O*-GlcNAcylation signaling pathways exhibited overlapping but distinct roles in the regulation of CSC-like phenotypes. Designing the most effective and appropriate strategy

towards the prevention and interception of such pro-tumorigenic signals may therefore contribute to the achievement of breast cancer elimination.

Conclusion

1. The essential enzymes in the HBP were up-regulated in breast cancer cells, which was in agreement with findings in human clinical samples.
2. *HAS2* gene was amplified and overexpressed in human breast cancers, particularly in aggressive type.
3. Co-expression of HAS2 and GFAT was correlated with poor prognosis in advance breast cancer patients and highly distributed in basal-like and claudin-low subtype which are markedly associated with cancer aggressiveness.
4. Inhibition of GFAT decreased CSC-like feature, along with the reduction of HA production and protein *O*-GlcNAcylation.
5. Gene targeting of Has2 significantly suppressed CSC-like phenotype and xenograft tumor growth.
6. Has2 deficiency attenuated the pro-tumorigenic Akt/GSK3β/β-catenin signal and anti-cancer drug resistance.
7. Pharmacological inhibition of protein *O*-GlcNAcylation reduced the CSC-like properties.
8. HA and *O*-GlcNAcylation signals play overlapping but distinct roles in the regulation of CSC-like phenotypes.

Table 1. Up-regulation of genes encoding HBP enzymes in clinical breast cancers

	GFAT1/GFAT2		GNPNAT1		PGM3		UAP1		References
	Fold	*p*-value	Fold	*p*-value	Fold	*p*-value	Fold	*p*-value	
Glück Breast									(Glück *et al*., 2012)
Invasive breast carcinoma	1.526 (154:4)	1.12e-4	1.687 (154:4)	0.016	n.s.		n.s.		
Radvanyi Breast									(Radvanyi *et al*., 2005)
Invasive ductal breast carcinoma	2.414 (30:6)	0.044	2.933 (31:5)	1.44e-5	n.s.		n.s.		
Invasive lobular breast carcinoma	4.491 (4:5)	0.046	1.937 (7:5)	0.040	n.s.		n.s.		
Finak Breast									(Finak *et al*., 2008)
Invasive breast carcinoma stroma	5.616† (53:6)	3.80e-14	1.761 (53:6)	2.55e-6	n.s.		n.s.		
Richardson Breast 2									(Richardson *et al*., 2006)
Ductal breast carcinoma	2.144 (40:7)	5.15e-7	n.s.		2.208 (40:7)	5.28e-5	1.608 (40:7)	0.012	
Ma Breast 4									(Ma *et al*., 2009)
Ductal breast carcinoma *in situ* epithelia	2.424 (9:14)	4.12e-6	1.738 (9:14)	4.29e-4	2.514 (9:14)	2.12e-5	1.968 (9:14)	0.007	
Ductal breast carcinoma *in situ* stroma	2.360† (11:14)	2.13e-5	n.s.		1.869 (11:14)	0.002	n.s.		
Invasive ductal breast carcinoma epithelia	1.595 (9:14)	0.008	n.s.		1.634 (9:14)	0.005	n.s.		
Invasive ductal breast carcinoma stroma	2.393† (9:14)	4.94e-4	n.s.		1.900 (9:14)	0.004	n.s.		

Curtis Breast								(Curtis *et al*., 2012)
Ductal breast carcinoma *in situ*	1.506 (10:144)	0.026	n.s.		1.600 (10:144)	3.50e-5	n.s.	
Medullary breast carcinoma	1.514 (32:144)	5.20e-10	n.s.		n.s.		n.s.	
Mucinous breast carcinoma	1.829 (46:144)	3.36e-13	n.s.		n.s.		n.s.	
Invasive breast carcinoma	1.640 (21:144)	8.10e-5	n.s.		1.658 (21:144)	6.90e-5	n.s.	
Invasive ductal breast carcinoma	1.528 (1,556:144)	4.48e-40	n.s.		n.s.		n.s.	
Invasive ductal and invasive lobular breast carcinoma	1.500 (90:144)	3.08e-14	n.s.		n.s.		n.s.	
Turashvili Breast								(Turashvili *et al*., 2007)
Invasive lobular breast carcinoma	2.238† (5:10)	0.044	n.s.		n.s.		n.s.	
TCGA Breast								(The Cancer Genome Atlas; http://tcga-data.nci.nih.gov/tcga/)
Mucinous breast carcinoma	1.982 (4:61)	0.013	n.s.		n.s.		1.613 (4:61)	8.14e-4
Mixed lobular and ductal breast carcinoma	n.s.		1.617 (7:61)	2.88e-4	n.s.		n.s.	
Male breast carcinoma	n.s.		1.917 (3:61)	0.005	n.s.		n.s.	
Invasive breast carcinoma	n.s.		1.735 (76:61)	1.21e-15	n.s.		n.s.	
Invasive ductal breast	n.s.		2.032	1.70e-29	n.s.		n.s.	

carcinoma			(389:61)					
Invasive lobular breast carcinoma	n.s.		1.565 (36:61)	2.13e-6	n.s.		n.s.	
Invasive ductal and lobular carcinoma	n.s.		1.633 (3:61)	0.006	n.s.		1.571 (3:61)	4.76e-4
Zhao Breast								(Zhao *et al*., 2004)
Lobular breast carcinoma	n.s.		n.s.		2.414 (18:3)	3.85e-7	1.721 (21:3)	4.05e-6
Invasive ductal breast carcinoma	n.s.		n.s.		1.667 (38:3)	4.53e-9	1.856 (37:3)	6.43e-8
Sørlie Breast 2								(Sørlie *et al*., 2003)
Ductal breast carcinoma	n.s.		n.s.		n.s.		1.644 (93:4)	0.028
Lobular breast carcinoma	n.s.		n.s.		n.s.		1.805 (7:4)	0.046
Sørlie Breast								(Sørlie *et al*., 2001)
Ductal breast carcinoma	n.s.		n.s.		n.s.		1.703 (65:4)	0.034

Genes exhibiting ≥ 1.5-log2 fold change of gene expression with *p*-value < 0.05 between breast cancer and normal samples in Oncomine databases (cDNA microarray analysis) are listed. † indicates the data of GFAT2. n.s; not significant. Numbers in parentheses indicate the number of cancer vs. normal samples.

Table 2. mRNA expression of HBP enzymes in primary breast cancer cells

Gene	MEC	MMTV-Neu cell	MMTV-PyVT cell
GFAT1	1.00 ± 0.17	1.25 ± 0.19	1.67 ± 0.19[b]
GFAT2	1.00 ± 0.30	n.d.	0.02 ± 0.01[b]
GNPNAT1	1.00 ± 0.18	1.39 ± 0.14[a]	1.42 ± 0.21[a]
PGM3	1.00 ± 0.22	1.64 ± 0.22[a]	2.81 ± 0.33[b,c]
UAP1	1.00 ± 0.08	1.11 ± 0.04	1.86 ± 0.23[b,d]

Relative ± SD fold change of mRNA expression of three independent experiments. [a] $p < 0.05$, [b] $p < 0.01$ compared with MEC. [c] $p < 0.05$, [d] $p < 0.01$ compared with MMTV-Neu cell. n.d.; not detected.

Table 3. Gene expression of *O*-GlcNAc cycling enzymes in clinical breast cancers

	OGT		OGA		References
	Fold	*p*-value	Fold	*p*-value	
Glück Breast					(Glück *et al*., 2012)
Invasive breast carcinoma	1.656 (154:4)	1.37e-4	n.s.		
Karnoub Breast					(Karnoub *et al*., 2007)
Invasive ductal breast carcinoma stroma	1.511 (7:15)	0.009	n.s.		
Curtis Breast					(Curtis *et al*., 2012)
Ductal breast carcinoma *in situ*	n.s.		-2.619 (10:144)	2.31e-7	
Benign breast neoplasm	n.s.		-2.336 (3:144)	0.02	
Breast carcinoma	n.s.		-2.039 (14:144)	7.04e-6	
Invasive breast carcinoma	n.s.		-2.018 (21:144)	2.23e-13	
Mucinous breast carcinoma	n.s.		-1.970 (46:144)	2.09e-20	
Medullary breast carcinoma	n.s.		-1.921 (32:144)	4.05e-13	
Invasive ductal breast carcinoma	n.s.		-1.849 (1,556:144)	3.69e-88	
Tubular breast carcinoma	n.s.		-1.788 (67:144)	9.31e-36	

Invasive ductal and invasive lobular breast carcinoma	n.s.	-1.784 (90:144)	1.06e-34	
Breast phyllodes tumor	n.s.	-1.703 (5:144)	0.021	
Invasive lobular breast carcinoma	n.s.	-1.650 (148:144)	2.10e-43	
Radvanyi Breast				(Radvanyi *et al*., 2005)
Invasive ductal breast carcinoma	n.s.	-1.841 (13:4)	0.050	
Richardson Breast 2				(Richardson *et al*., 2006)
Ductal breast carcinoma	n.s.	-1.773 (40:7)	3.17e-7	
TCGA Breast				(The Cancer Genome Atlas; http://tcga-data.nci.nih.gov/tcga/)
Invasive breast carcinoma	n.s.	-1.766 (76:61)	1.05e-10	
Invasive ductal breast carcinoma	n.s.	-1.684 (389:61)	4.41e-13	

Genes exhibiting ≥ 1.5-log2 fold change of gene expression with *p*-value < 0.05 between breast cancer and normal samples in Oncomine databases (cDNA microarray analysis) are listed. n.s; not significant. Numbers in parentheses indicate the number of cancer vs. normal samples.

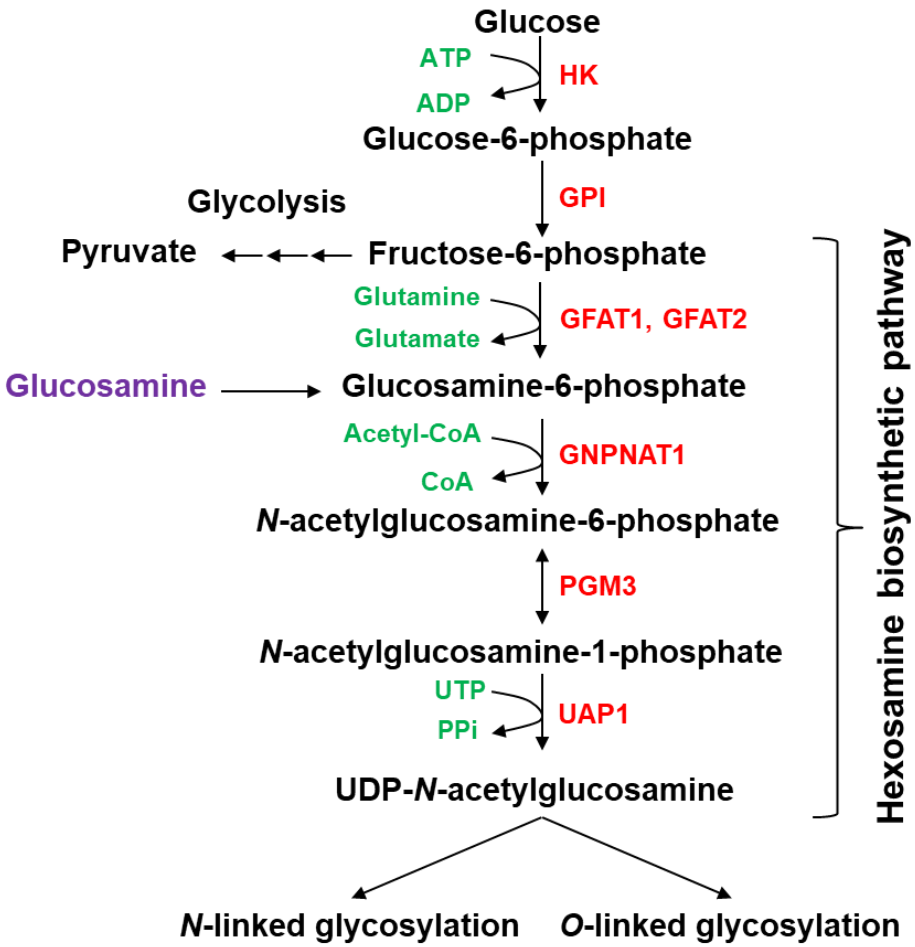

Figure 1. Hexosamine biosynthetic pathway. Glucose is phosphorylated by hexokinase (HK) and then converted to fructose-6-phosphate by glucose-6-phosphate isomerase (GPI). The glutamine:fructose-6-phosphate amidotransferase (GFAT), a rate limiting enzyme of the HBP, utilizes the glutamine as an amine donor to generate glucosamine-6-phosphate. In the next step, acetyl-CoA is transferred to glucosamine-6-phosphate by glucosamine-phosphate *N*-acetyltransferase 1 (GNPNAT1). The resulting *N*-acetylglucosamine-6-phosphate is then converted to *N*-acetylglucosamine-1-phosphate by phosphoglucomutase 3 (PGM3). In the final step, the uridine-5'-triphosphate (UTP) is transferred to GlcNAc-1-phosphate by UDP-*N*-acetylglucosamine pyrophosphorylase (UAP1) to form the end products UDP-*N*-acetylglucosamine.

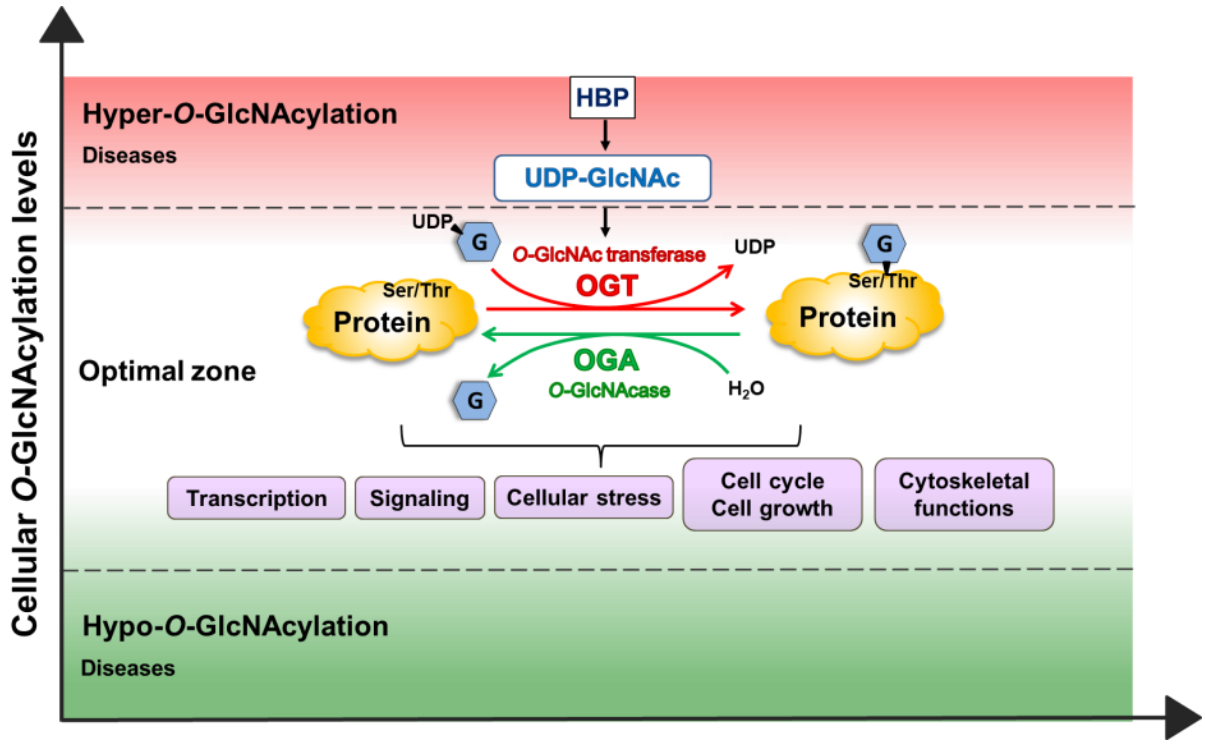

Figure 2. Protein *O*-GlcNAcylation. *O*-GlcNAcylation is an essential post-translational modification. *O*-GlcNAc is a dynamic cycles that rapidly changes in response to the metabolic alteration and environmental signals. *O*-GlcNAcylation is regulated by two enzymes: *O*-GlcNAc transferase (OGT) catalyzes the addition of *O*-GlcNAc moiety from the high-energy intermediate UDP-GlcNAc to the serine (Ser) or threonine (Thr) residues of target protein, while *O*-GlcNAcase (OGA) is responsible for removing *O*-GlcNAc. This modification is implicate in a broad spectrum of intracellular proteins in which can affect to various biological processes such as transcription, translation, signal transduction, metabolism and proteasomal degradation (Hart, 2014; Bond and Hanover, 2015). There are more than 3,000 proteins that could be modulated by *O*-GlcNAcylation (Groves *et al.*, 2013). Dysregulation of *O*-GlcNAc cycling leads to several diseases including diabetes, cardiovascular disease, neurological disorders, and cancers.

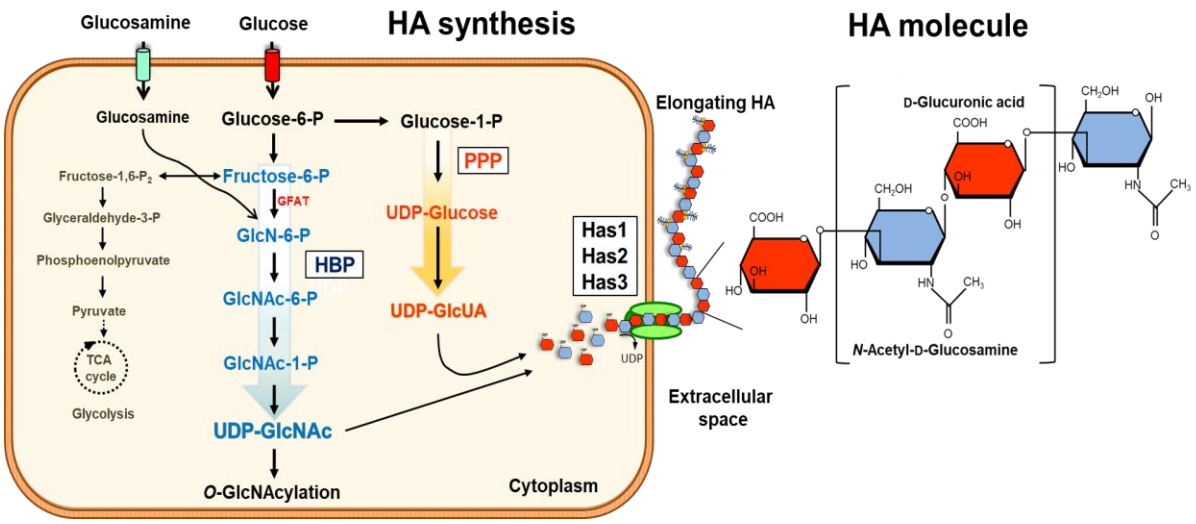

Figure 3. Hyaluronan synthesis. HA is a linear polysaccharide and major constituent of the extracellular microenvironment. HA biosynthesis is regulated by three HA synthases (Has1–3) that serve to link UDP-GlcNAc and UDP-glucuronic acid (UDP-GlcUA) substrates together in alternating β-1,3 and β-1,4 linkages.

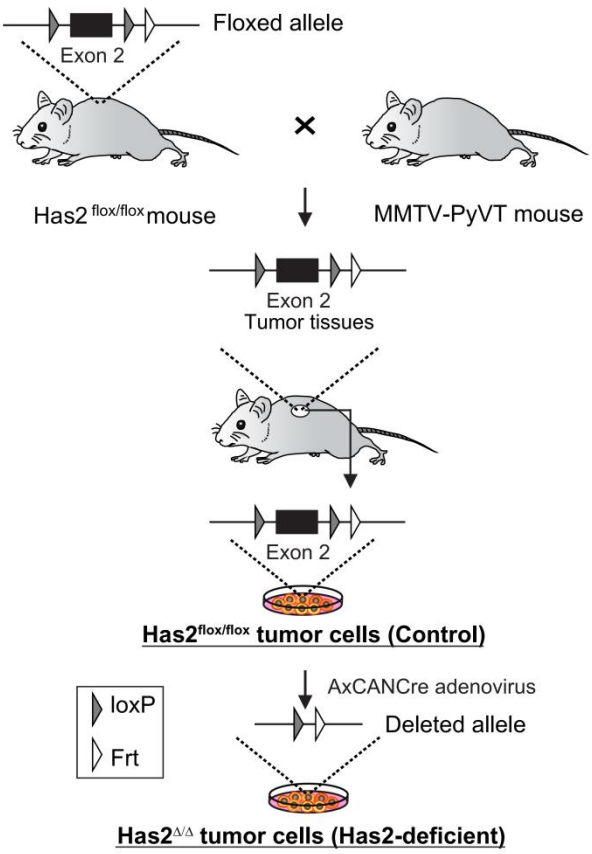

Figure 4. Schematic representation of Has2-deficient breast carcinoma cells. Targeted disruption of the mouse *Has2* gene in breast carcinoma cells. $Has2^{flox/flox}$ mice were back-crossed to MMTV-PyVT mice to generate mammary tumor model mice. $Has2^{flox/flox}$ tumor cells were established from primary mammary tumors of $Has2^{flox/flox}$ tumor model mice and infected with the AxCANCre adenovirus carrying the Cre recombinase to generate Has2-deficient $Has2^{\Delta/\Delta}$ cells. Exon 2 of the Has2 locus was flanked by two loxP sites in a floxed allele and was deleted by Cre-mediated recombination in a deleted allele. The knockout efficiency of Has2 was further evaluated by the measurement of Has2 expression and HA production using qRT-PCR and ELISA-like assay, respectively.

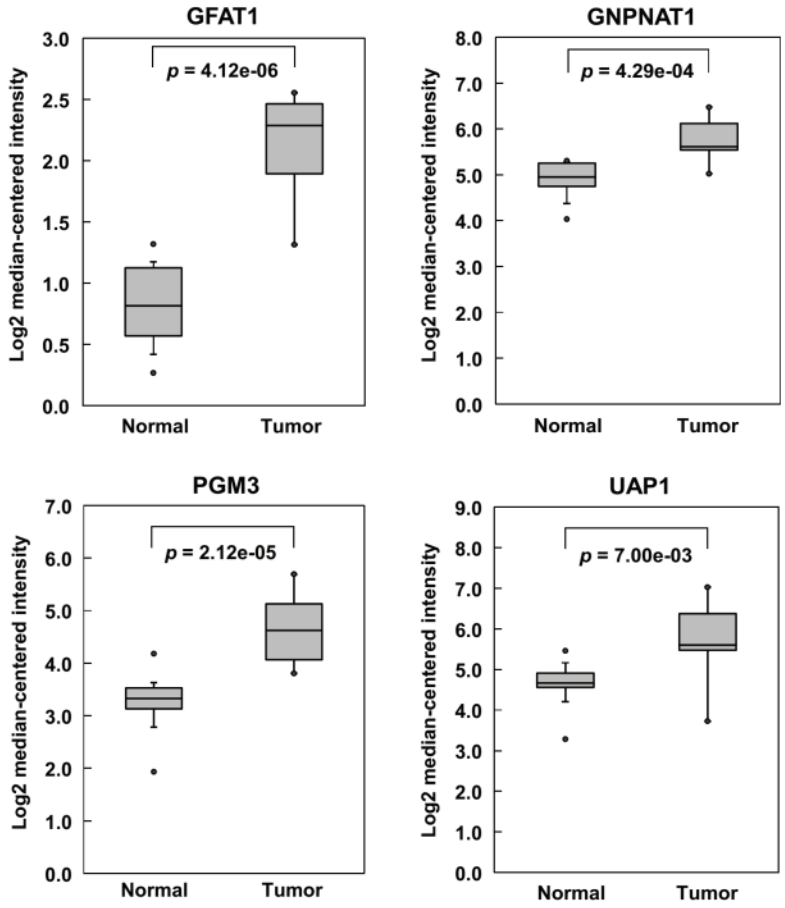

Figure 5. Up-regulation of HBP-related genes in clinical breast cancer using Oncomine database. The mRNA expression of the HBP genes *GFAT1*, *GNPNAT1*, *PGM3*, and *UAP1* was analyzed using the Oncomine database (Ma Breast 4 dataset). Box-plot diagrams display comparisons of target gene expression between the normal group (left plot) and the ductal breast carcinoma *in situ* epithelia group (right plot). The upper and lower boundaries of boxes represent the 75% and 25% quartiles, respectively. The line in the middle of boxes shows the median value and dots extend from the quartiles to the respective maximum and minimum values. The two-tailed Student's *t*-test was used to ascertain statistically significant differences between the groups.

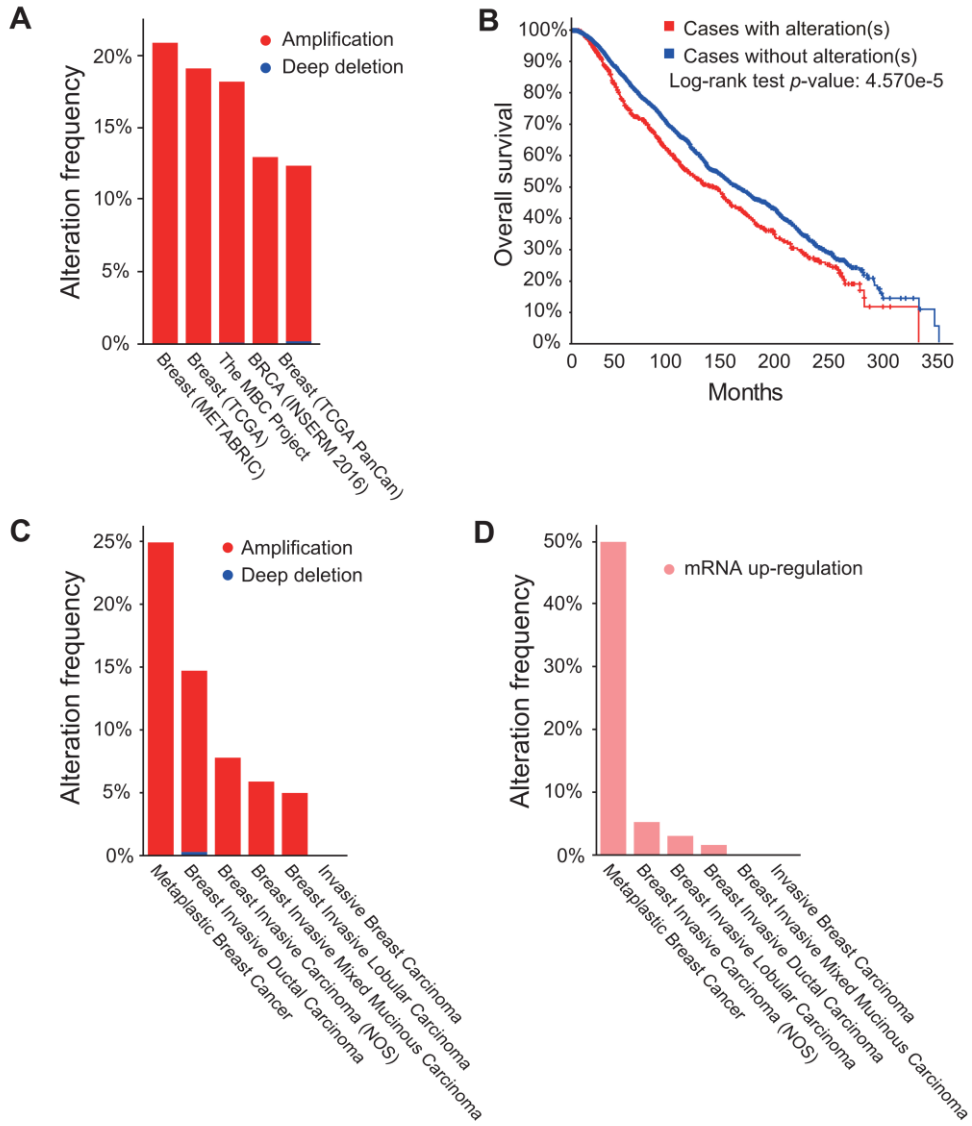

Figure 6. Gene amplification of *HAS2* in aggressive breast cancers. **A** Gene amplification of *HAS2* in clinical breast cancers (data from TCGA Research Network) and **B** Kaplan–Meier curves for overall survival in patients with and without gene amplification. The total number of analyzed samples was 5071 for gene amplification and overall survival. Raw *p*-values were calculated by the log-rank test. **C** Copy number of *HAS2* within different cancer types from TCGA PanCancer Atlas dataset (n = 1070). **D** The mRNA expression of HAS2 within different cancer types from TCGA PanCancer Atlas dataset (n = 1070).

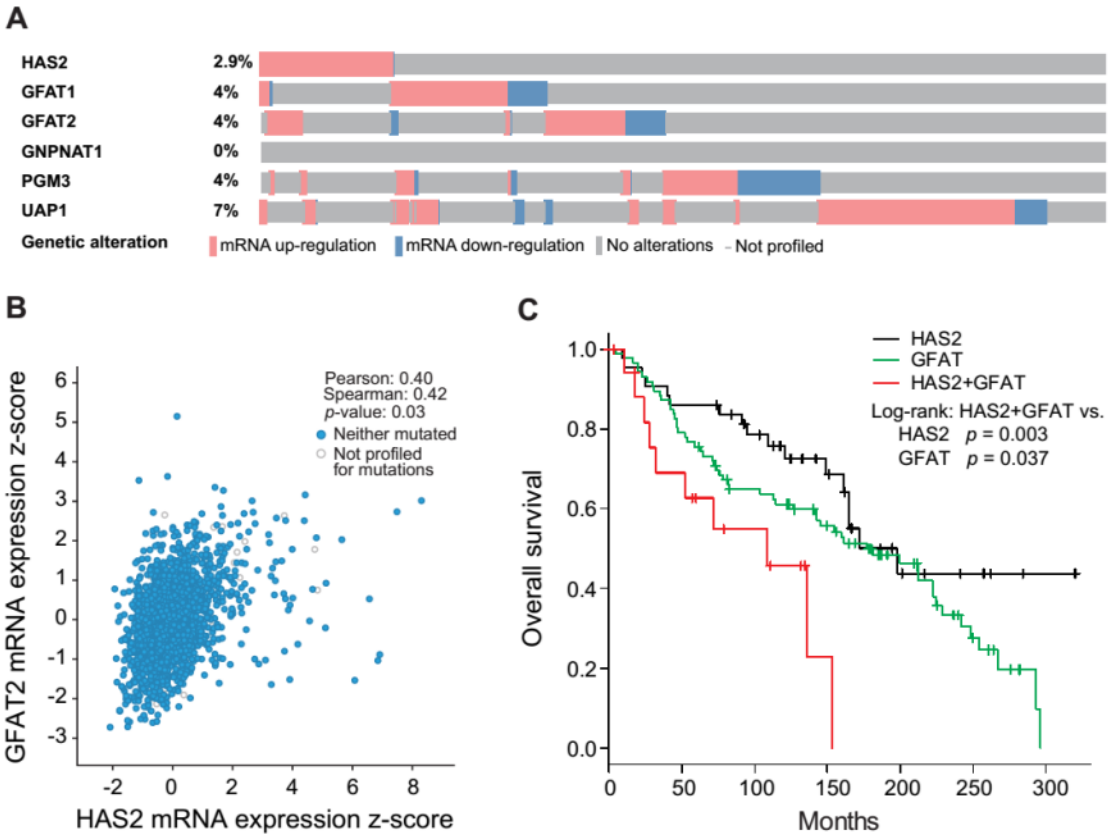

Figure 7. Co-expression of GFAT and HAS2 in breast cancer patients. **A** The mRNA expression data of HBP and *HAS2* genes were extracted from TCGA METABRIC datasets through cBioPortal and presented as OncoPrint for 2509 cases. Color coding indicates gene expression (pink: up-regulation, blue: down-regulation). **B** TCGA analysis of the correlation between the expression of HAS2 and GFAT2. **C** Overall survival curves of breast cancer patients categorized according to the expression of HAS2 and GFAT (GFAT1 and 2). The $HAS2^{high}$/$GFAT^{high}$ group (HAS2+GFAT: n = 18) was compared with the $HAS2^{high}$ group (HAS2: n = 44) or $GFAT^{high}$ group (GFAT: n = 86).

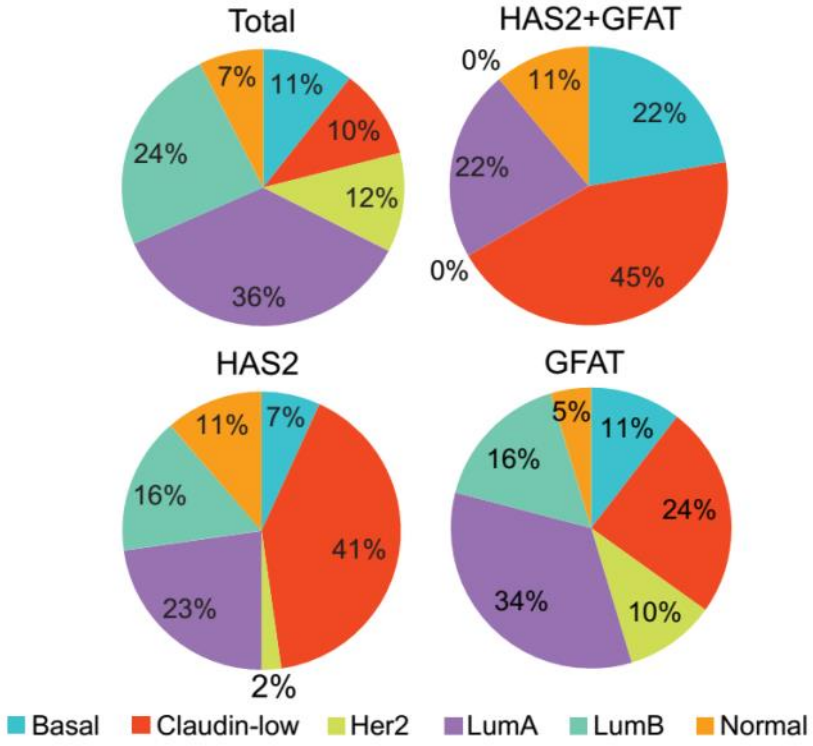

Figure 8. Distribution of the intrinsic molecular subtypes of breast cancer for HAS2 and GFAT mRNA expression. The prediction of intrinsic molecular subtype was performed using the METABRIC dataset**.** HAS2 positivity was enriched in the most aggressive subtypes, basal-like and claudin-low, and more prominent in combination with GFAT positivity (n = 1898 in total, 44 in HAS2, 86 in GFAT, and 18 in HAS2+GFAT). Basal (Basal-like), Claudin-low, Her2 (Her2-enriched), LumA (Luminal A), LumB (Luminal B), and Normal (Normal breast-like).

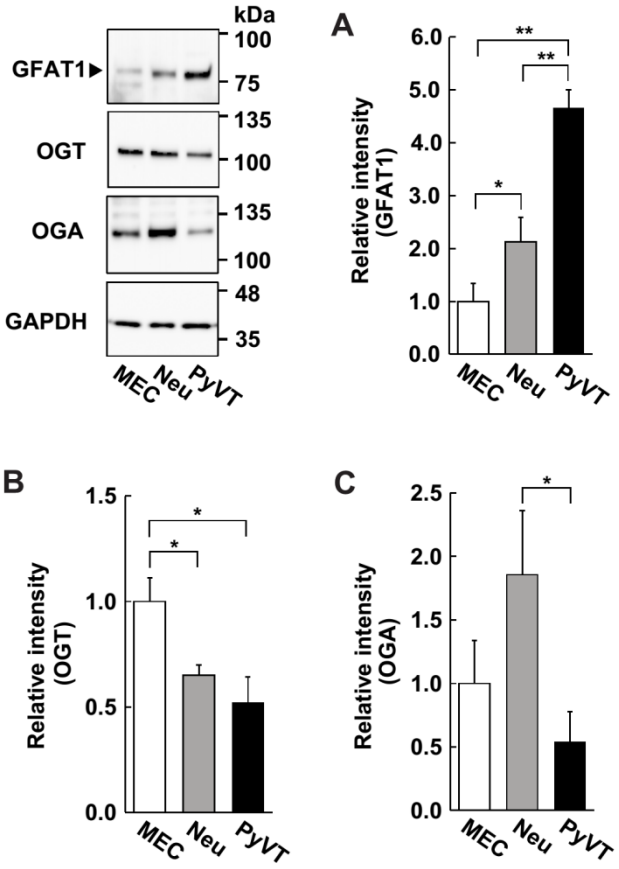

Figure 9. GFAT1 and *O*-GlcNAc cycling genes expression in primary breast cancer cells. Relative protein expression of key regulator of HBP, **(A)** GFAT1 and *O*-GlcNAc cycling enzymes **(B)** OGT and **(C)** OGA, were analyzed in mammary epithelial cells (MECs) and MMTV-Neu (Neu) and MMTV-PyVT (PyVT) cancer cells by western blot analysis. GAPDH was used as an internal control. Band intensities were quantified by densitometric analysis using ImageJ software and standardized with respect to GAPDH. All data represent the mean ± S.D. of three independent experiments. *, $p < 0.05$; **, $p < 0.01$.

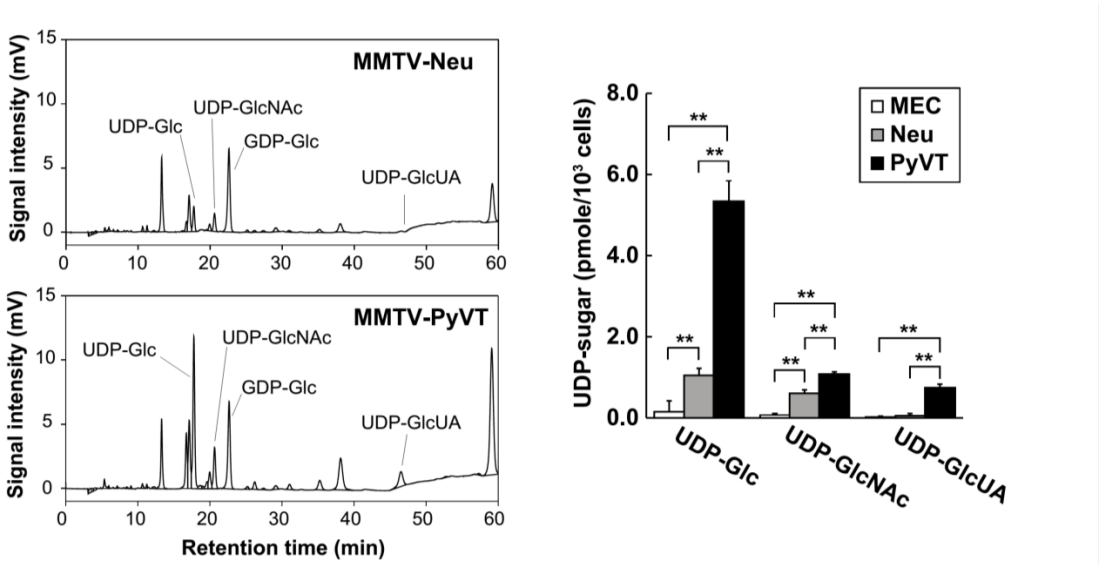

Figure 10. Quantitative analysis of nucleotide sugars in primary breast cancer cells using High-performance liquid chromatography. Cells lysate ($3x10^5$-$5x10^5$ cells) were lysed with ice-cold 70% ethanol. After purify with ion-pair solid phase extraction, samples were lyophilized and dissolved in water (50 µl). The 20 µl of each sample was injected into the column. Cellular levels of nucleotide sugar production in MECs, Neu and PyVT cells were monitored using HPLC. The amount of nucleotide sugars in samples were calculated by linear regression of standards curve and reported as pmole/10^3 cells unit. Data represent the mean ± S.D. of three independent experiments. **, $p < 0.01$.

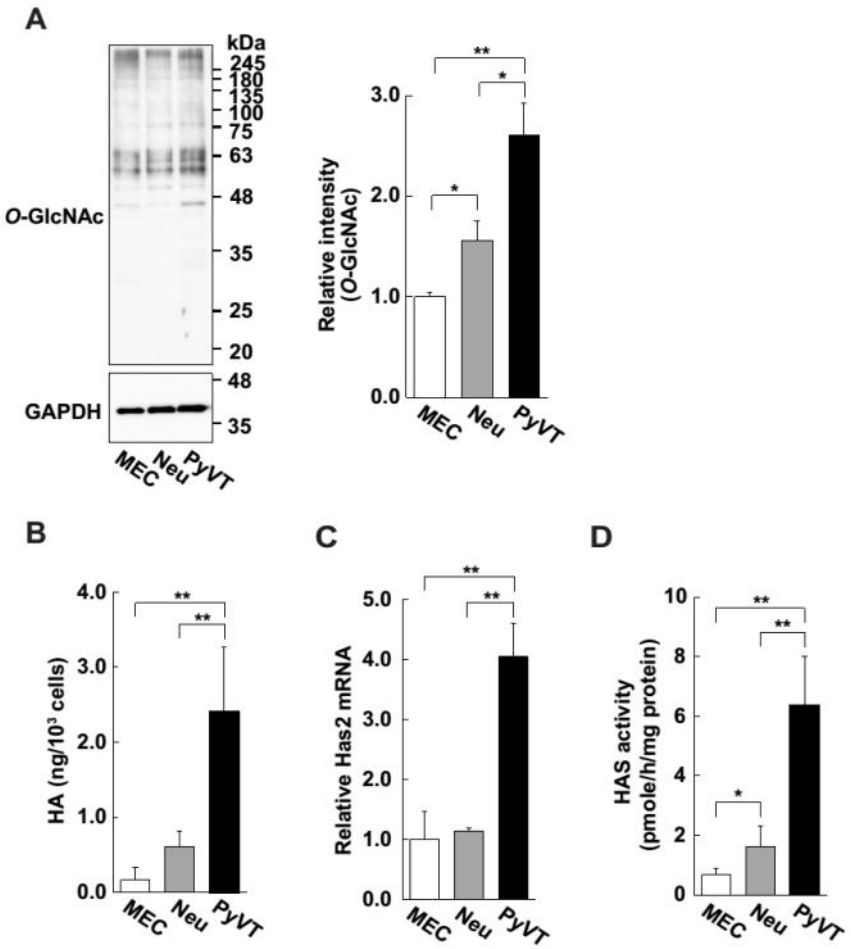

Figure 11. Protein *O*-GlcNAcylation and HA production in primary breast cancer cells. **A** Cell lysates from MECs, Neu and PyVT cells were subjected to western blot analysis to examine the levels of total protein *O*-GlcNAcylation. GAPDH was used as an internal control. Band intensities were quantified by densitometric analysis using ImageJ software and standardized with respect to GAPDH. **B** HA contents in the conditioned medium of MECs, Neu and PyVT cells were analyzed by a competitive ELISA-like assay. Data represent the mean ± S.D. of six independent experiments. **C** Relative expression of Has2 mRNA was analyzed by qRT-PCR. Data represent the mean ± S.D. of three independent experiments**. D** HAS activity was determined as described in the Materials and Methods. Data represent the mean ± S.D. of three independent experiments. *, $p < 0.05$; **, $p < 0.01$.

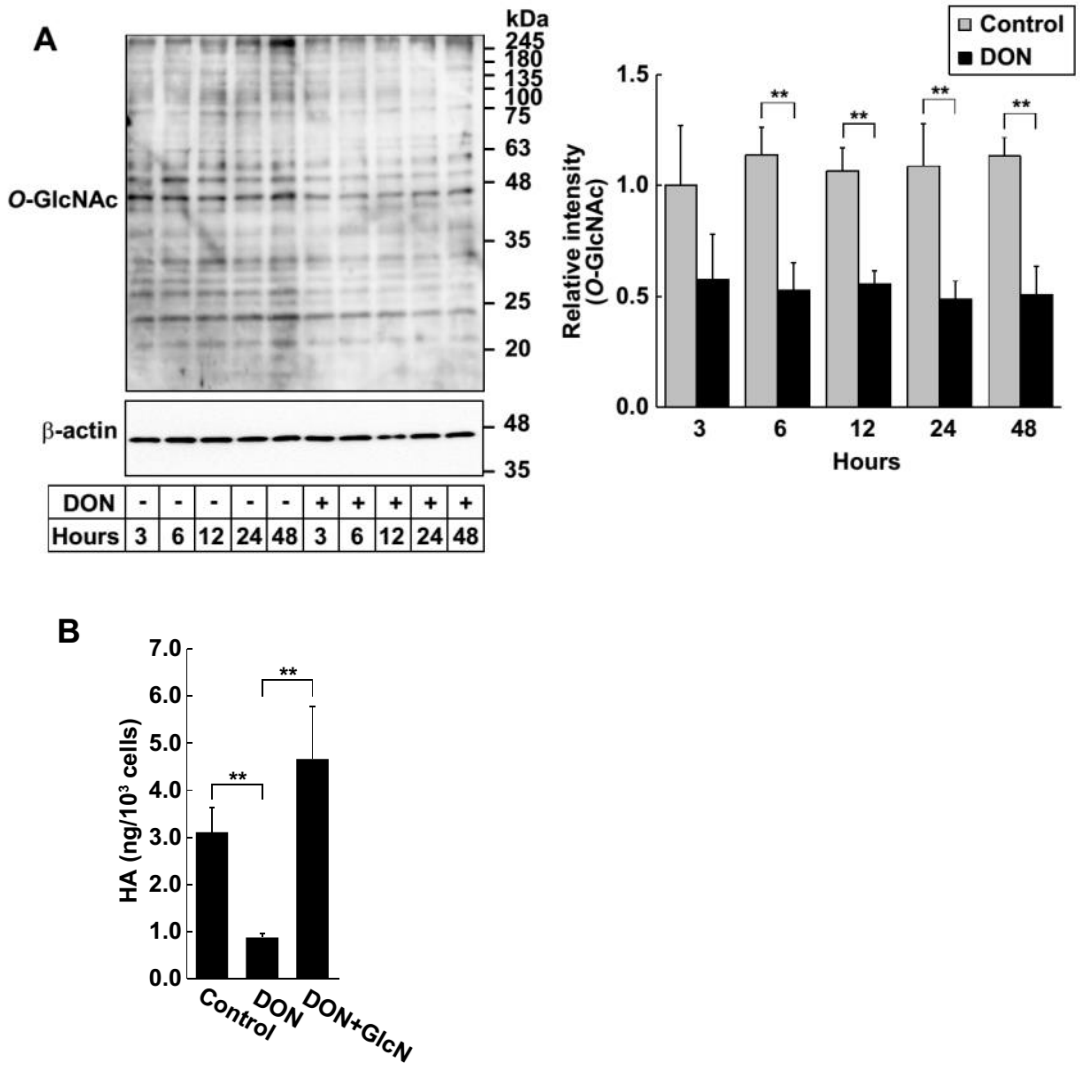

Figure 12. HBP flux regulates *O*-GlcNAcylation and HA production. **A** Western blot analysis for protein *O*-GlcNAcylation after GFAT inhibition. MMTV-PyVT cancer cells were treated with 20 μM DON (GFAT inhibitor) for the indicated times (3–48 h). Band intensities were quantified by densitometric analysis using ImageJ software and standardized with respect to a β-actin internal control. Data represent the mean ± S.D. of three independent experiments. **, $p < 0.01$ versus untreated control cells. **B** HA content in the conditioned medium of MMTV-PyVT cancer cells was measured by a competitive ELISA-like assay. The cells were treated with 20 μM DON alone or combination with 200 μM D-Glucosamine (GlcN) for 48 h. Data represent the mean ± S.D. of three independent experiments. **, $p < 0.01$.

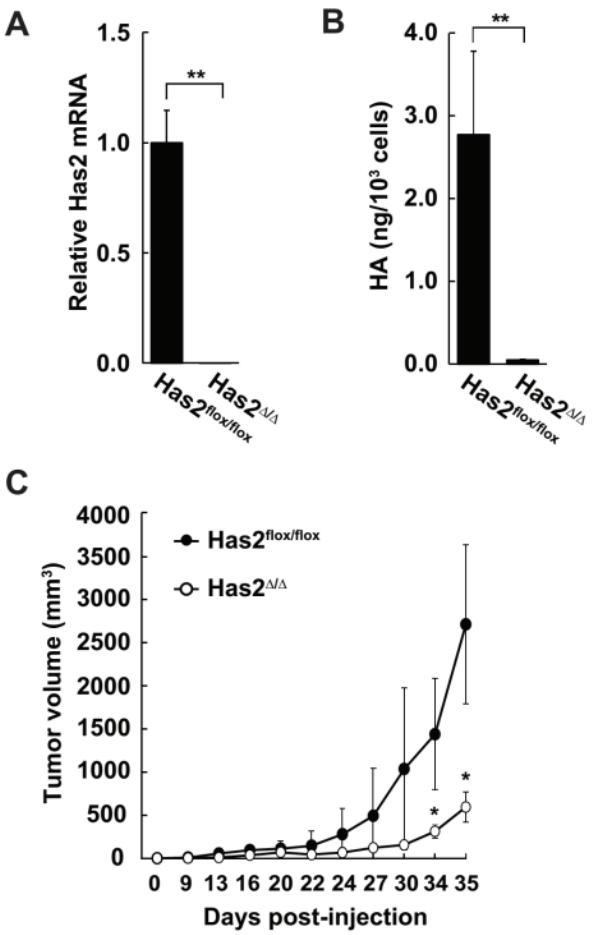

Figure 13. A deficiency in tumoral HA biosynthesis suppresses xenograft tumor growth. **A** Has2 expression and HA production in Has2-deficient breast cancer cells. Total RNA samples isolated from Has2-deficient $Has2^{\Delta/\Delta}$ and control $Has2^{flox/flox}$ cells were subjected to qRT-PCR. The expression of Has2 was almost completely suppressed in $Has2^{\Delta/\Delta}$ cells. **B** HA content in the conditioned medium of $Has2^{\Delta/\Delta}$ and $Has2^{flox/flox}$ cells was measured by a competitive ELISA-like assay. HA content was markedly diminished in Has2-deficient $Has2^{\Delta/\Delta}$ cells. Data represent the mean ± S.D. of three independent experiments. **, $p < 0.01$ versus control $Has2^{flox/flox}$ cells. **C** Xenograft tumor growth of Has2-deficient breast cancer cells. Has2-deficient $Has2^{\Delta/\Delta}$ and control $Has2^{flox/flox}$ cells were subcutaneously inoculated at 1×10^6 cells into BALB/c nude mice. Tumor volume was measured every 2 to 4 days for 35 days. The tumor volume was calculated formula: volume = $(\text{width})^2 \times \text{length}/2$. Data represent the mean ± S.D. (n = 6). *, $p < 0.05$ versus control $Has2^{flox/flox}$ cells.

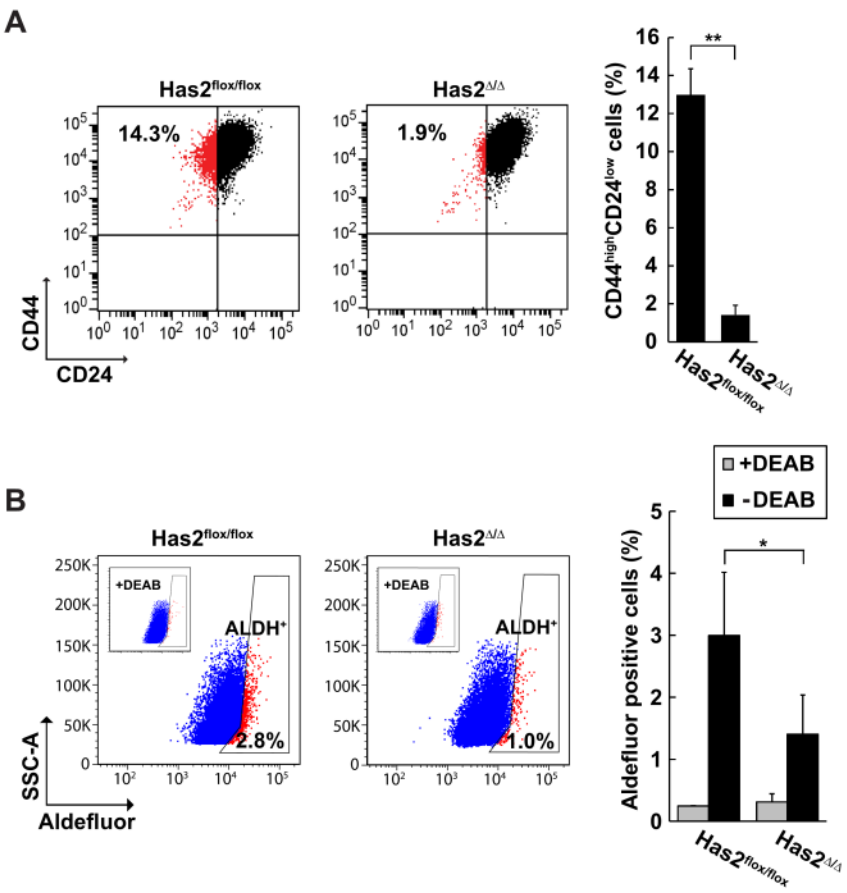

Figure 14. Deletion of Has2 attenuates CSC-like phenotypes. A Flow cytometric analysis of the $CD44^{high}/CD24^{low}$ subpopulation in Has2-deficient $Has2^{\Delta/\Delta}$ breast cancer cells and control $Has2^{flox/flox}$ cells. Data represent the mean ± S.D. of three independent experiments. **, $p < 0.01$. **B** Percentage of ALDH positive population of Has2-deficient $Has2^{\Delta/\Delta}$ and control $Has2^{flox/flox}$ cells were identified using a flow cytometry-based Aldefluor assay. Baseline fluorescence was established in the presence of ALDH inhibitor DEAB (insets). Data represent the mean ± S.D. of four independent experiments. *, $p < 0.05$.

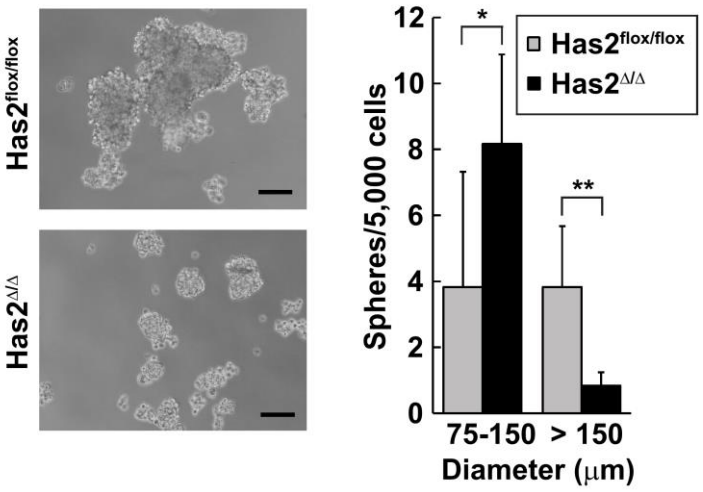

Figure 15. Has2 knockout suppresses the mammosphere-forming ability. Mammosphere formation of Has2-deficient $Has2^{\Delta/\Delta}$ and control $Has2^{flox/flox}$ cells. Representative images of mammospheres were taken and mammosphere number was counted under a phase-contrast microscope. Scale bar: 100 μm. Data represent the mean ± S.D. of six independent experiments. *, $p < 0.05$, **, $p < 0.01$.

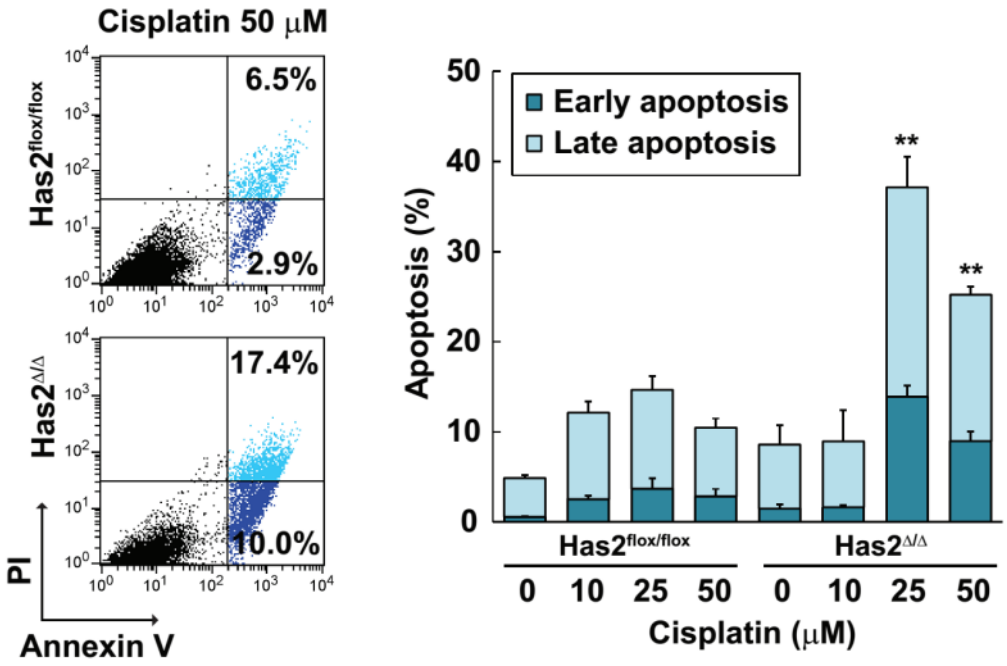

Figure 16. Effect of Has2-deficient on cisplatin-induced apoptosis in primary breast cancer cells. Has2-deficient Has2$^{\Delta/\Delta}$ and control Has2$^{flox/flox}$ cells were treated with 0-50 μM cisplatin for 16 h. Treated cells were stained with fluorescent Annexin V and PI and then analyzed by flow cytometry. Early and late apoptotic cells were represented as Annexin V^{+}/PI^{-} or Annexin V^{+}/PI^{+} subpopulation, respectively. Data represent the mean ± S.D. of four independent experiments. **, $p < 0.01$ Has2$^{\Delta/\Delta}$ versus control Has2$^{flox/flox}$ cells.

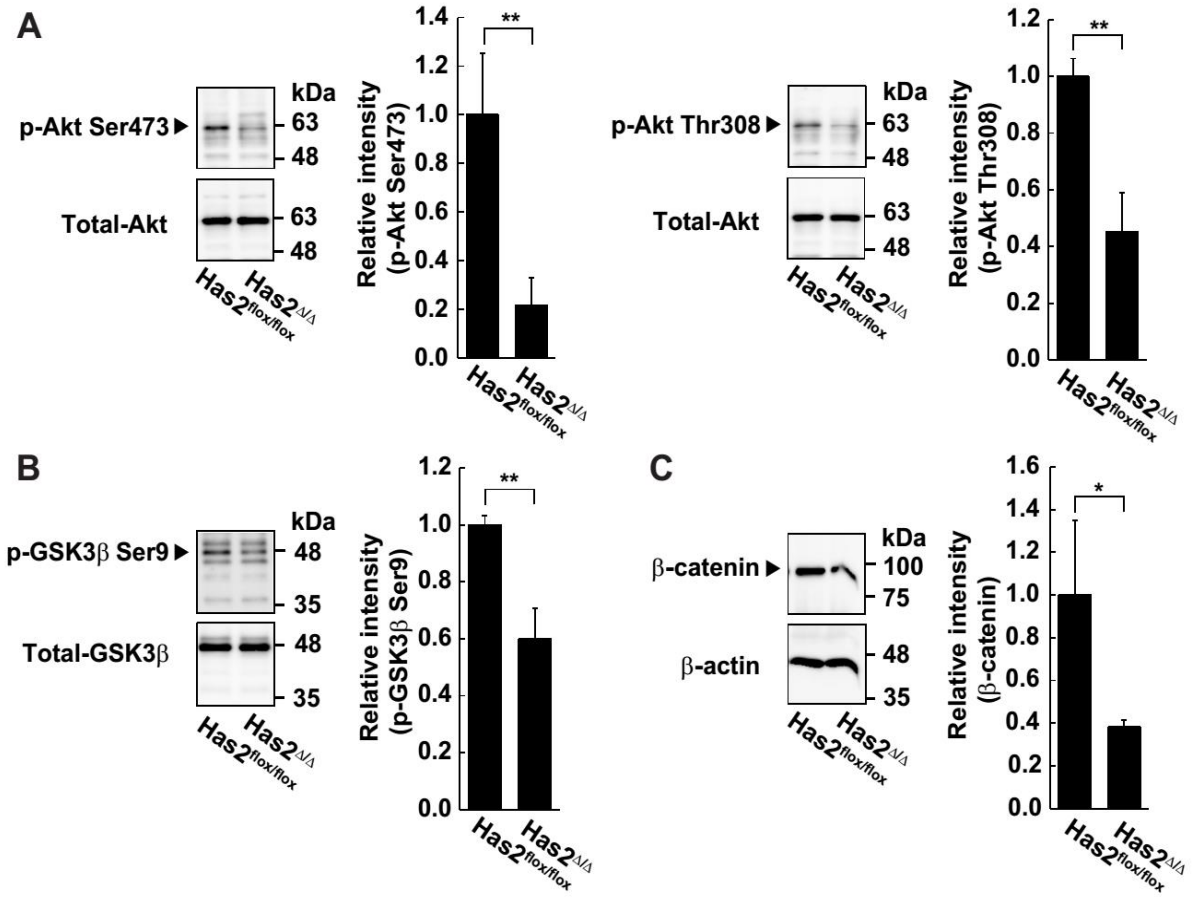

Figure 17. HA triggers the pro-oncogenic signals. Has2-deficient $Has2^{\Delta/\Delta}$ and control $Has2^{flox/flox}$ cells were grown in 10% dialyzed FBS/DMEM for 48 h. Western blot analysis was conducted to determine the expression of **(A)** phospho-Akt Ser473 (left) and phospho-Akt Thr308 (right), **(B)** phospho-GSK3β Ser9, and **(C)** β-catenin. Total Akt, total GSK3β, or β-actin was used as an internal control. Band intensities were quantified by densitometric analysis using ImageJ software. Data represent the mean ± S.D. of three independent experiments. *, $p < 0.05$; **, $p < 0.01$.

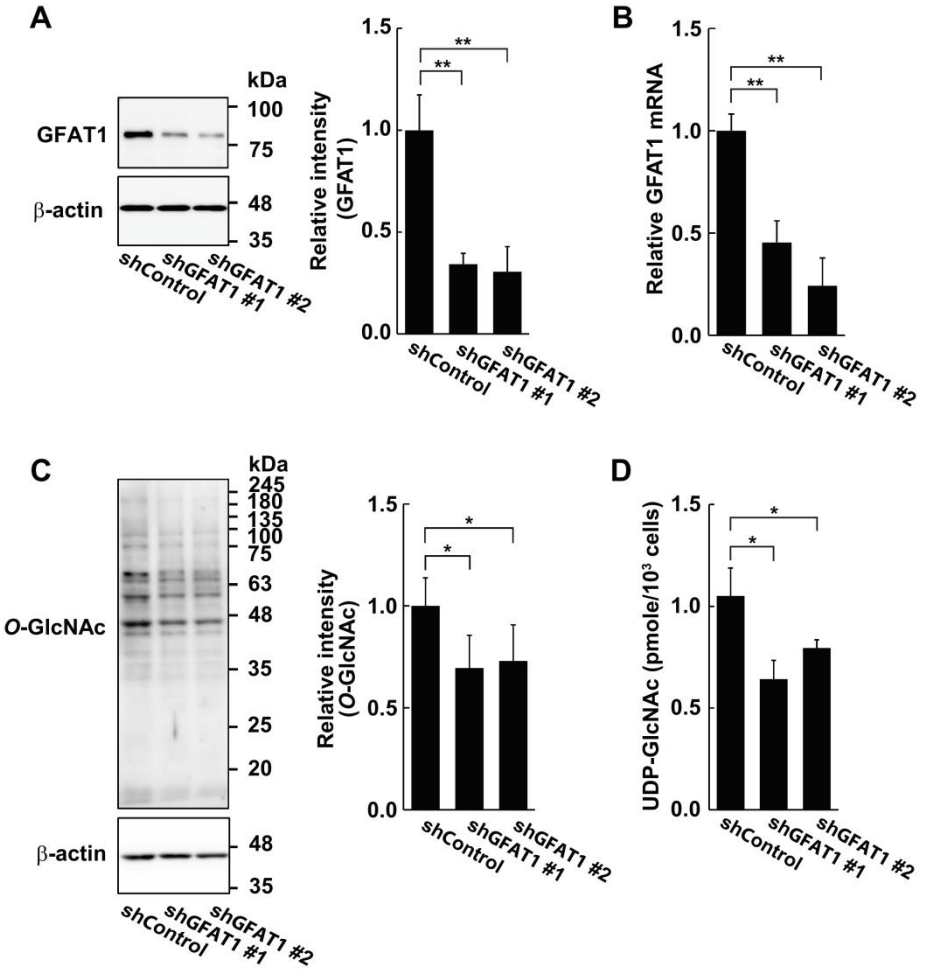

Figure 18. Alteration of protein *O*-GlcNAcylation and UDP-GlcNAc levels in GFAT1 knockdown cells. GFAT1 knockdown Has2$^{flox/flox}$ cells were generated by transfection of lentivirus carrying GFAT1 shRNA and designated as shGFAT1 #1 and #2. Control cells were generated by a transfection of non-targeting shRNA and designated as shControl. **A** Cell lysates were analyzed by western blotting with anti-GFAT1 and anti-β-actin antibodies. **B** Relative expression of GFAT1 mRNA was evaluated by qRT-PCR. Data represent the mean ± S.D. of three independent experiments. **C** Western blot analysis for protein *O*-GlcNAcylation in GFAT knockdown and control cells. Data represent the mean ± S.D. of five independent experiments. **D** HPLC analysis of cellular UDP-GlcNAc levels. Data represent the mean ± S.D. of three independent experiments**.** *, $p < 0.05$, **, $p < 0.01$.

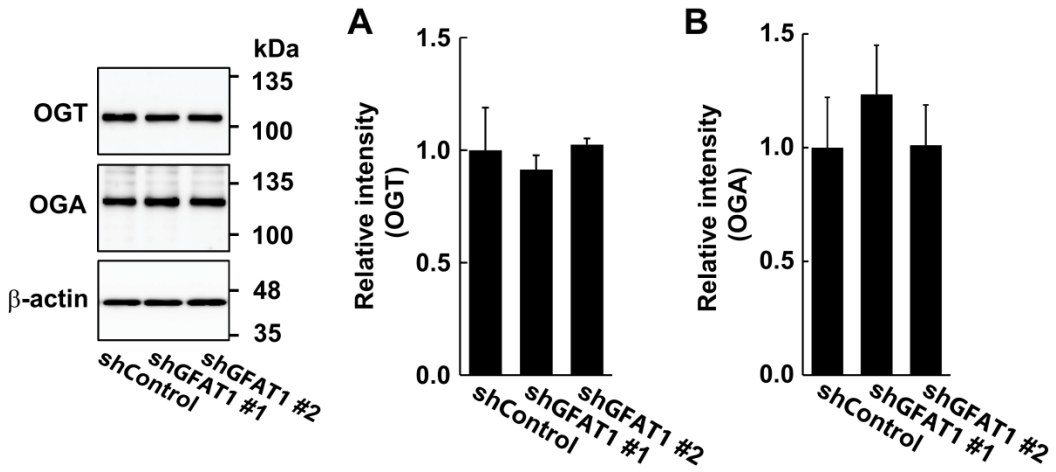

Figure 19. Expression levels of *O*-GlcNAc cycling enzymes in GFAT1 knockdown cells. GFAT1 knockdown cells were cultured in DMEM supplemented with 10% FBS for 48 h and then whole cell lysates were subjected to SDS–PAGE. **(A)** OGT and **(B)** OGA protein expression were analyzed by western blotting. β-actin was used as a loading control. Band intensities were quantified by densitometric analysis using ImageJ software and standardized with respect to β-actin. Data represent the mean ± S.D. of three independent experiments.

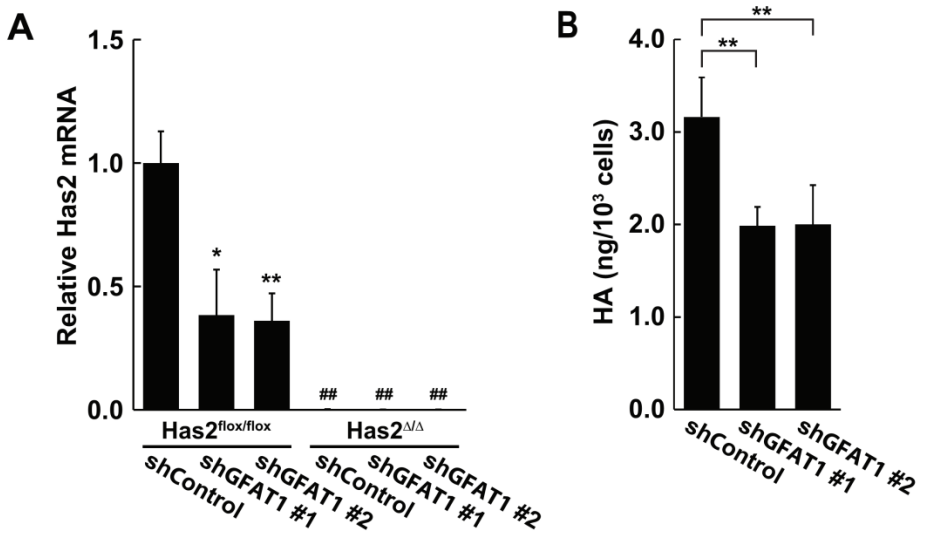

Figure 20. GFAT1 knockdown decreases Has2 mRNA expression and HA production. A Relative expression of Has2 mRNA was analyzed by qRT-PCR. Data represent the mean ± S.D. of three independent experiments. *, $p < 0.05$; **, $p < 0.01$ versus shControl. ##, $p < 0.01$ versus corresponding control $Has2^{flox/flox}$ cell. **B** Cells were cultured in 10%FBS-DMEM for 48 h, the conditioned medium were collected and measured the HA levels by a competitive ELISA-like assay. Data represent the mean ± S.D. of four independent experiments. **, $p < 0.01$ versus shControl.

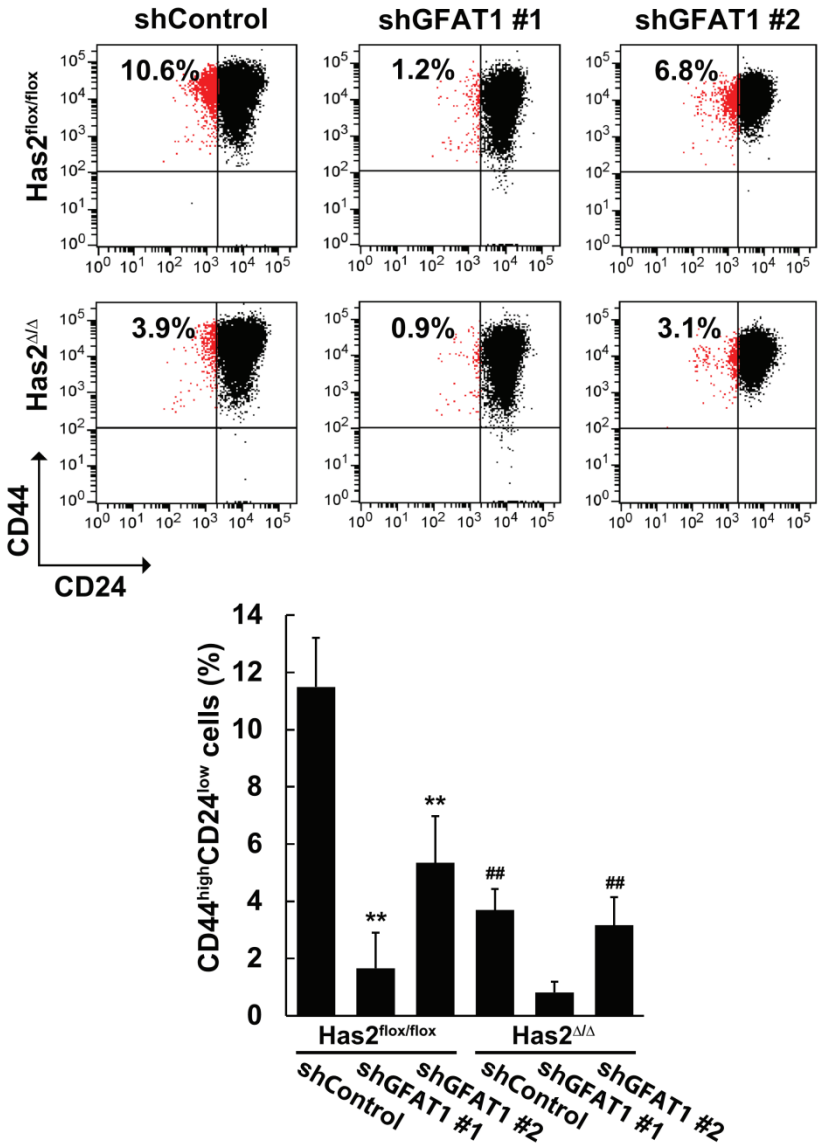

Figure 21. Coordinated action of GFAT and Has2 on CSC-like feature. Flow cytometric analysis of the $CD44^{high}/CD24^{low}$ subpopulation in GFAT1 knockdown/Has2-deficient cells. CD24 and CD44 expression in GFAT1 knockdown cells was analyzed before and after Has2 deletion by flow cytometry. Data represent the mean ± S.D. of seven independent experiments. **, $p < 0.01$ versus shControl. ##, $p < 0.01$ versus corresponding control $Has2^{flox/flox}$ cell.

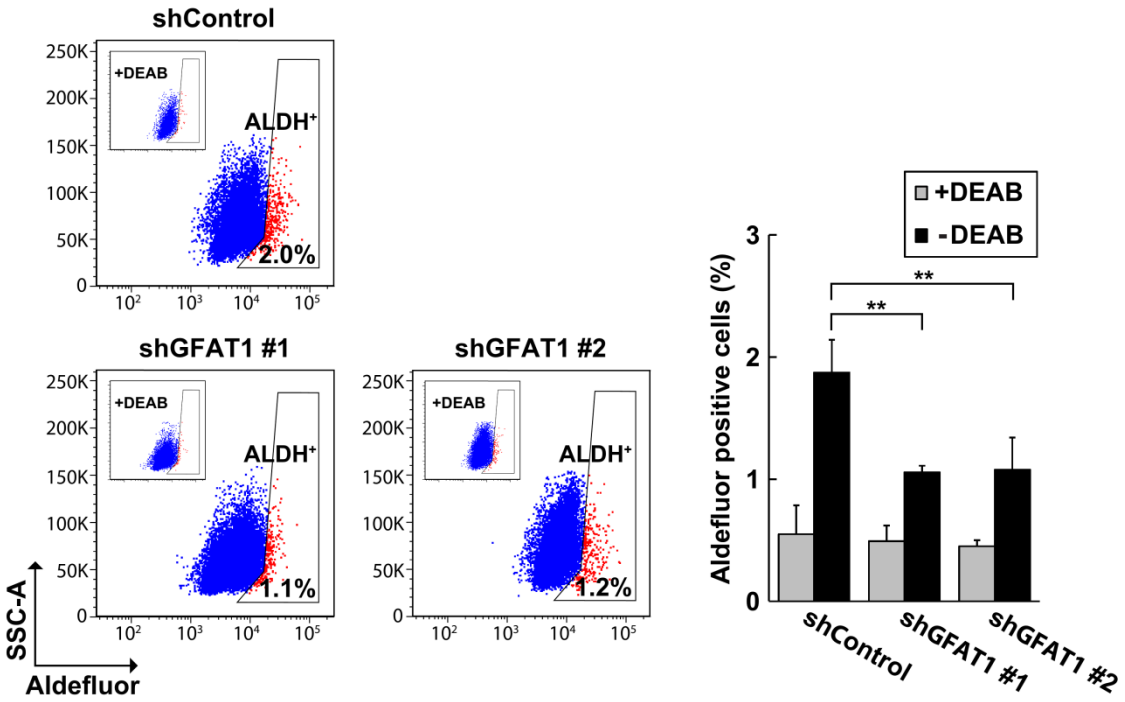

Figure 22. Representative flow cytometric histograms of ALDH expression after silencing GFAT1. The GFAT knockdown (shGFAT1 #1 and #2) and control (shControl) cells were examined the ALDH activity. $ALDH^+$ cells were identified using a flow cytometry-based Aldefluor assay. Baseline fluorescence was established in the presence of ALDH inhibitor DEAB (insets). Data represent the mean ± S.D. of four independent experiments. **, $p < 0.01$.

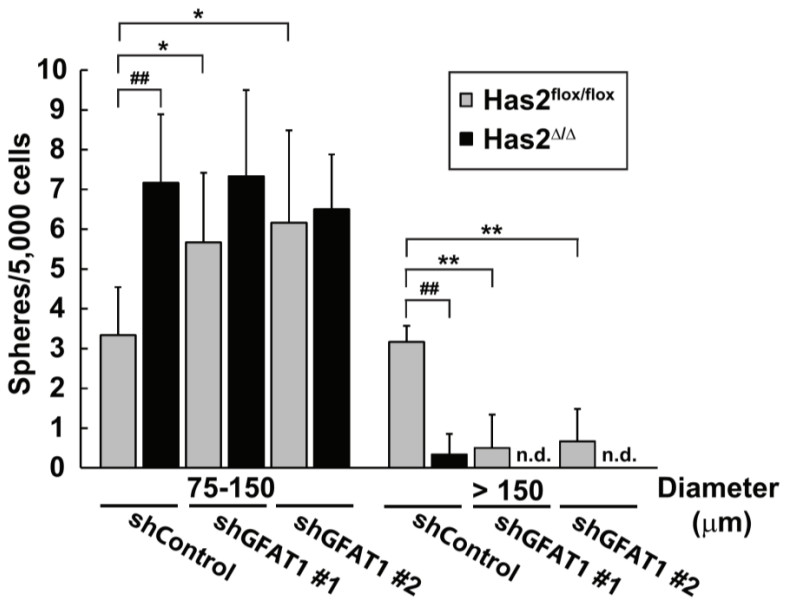

Figure 23. Effect of silencing GFAT and Has2 on mammosphere formation. Mammosphere formation of GFAT1 knockdown/Has2-deficient cells. The 5,000 of each cell was seeded in a 24-well low-attachment plate with conditioned media for 7 days. Representative images of mammospheres were taken and mammosphere number was counted under a phase-contrast microscope. Scale bar: 100 μm. Data represent the mean ± S.D. of six independent experiments. *, $p < 0.05$; **, $p < 0.01$ versus shControl. ##, $p < 0.01$ versus corresponding control $Has2^{flox/flox}$ cell. n.d.; non-detected.

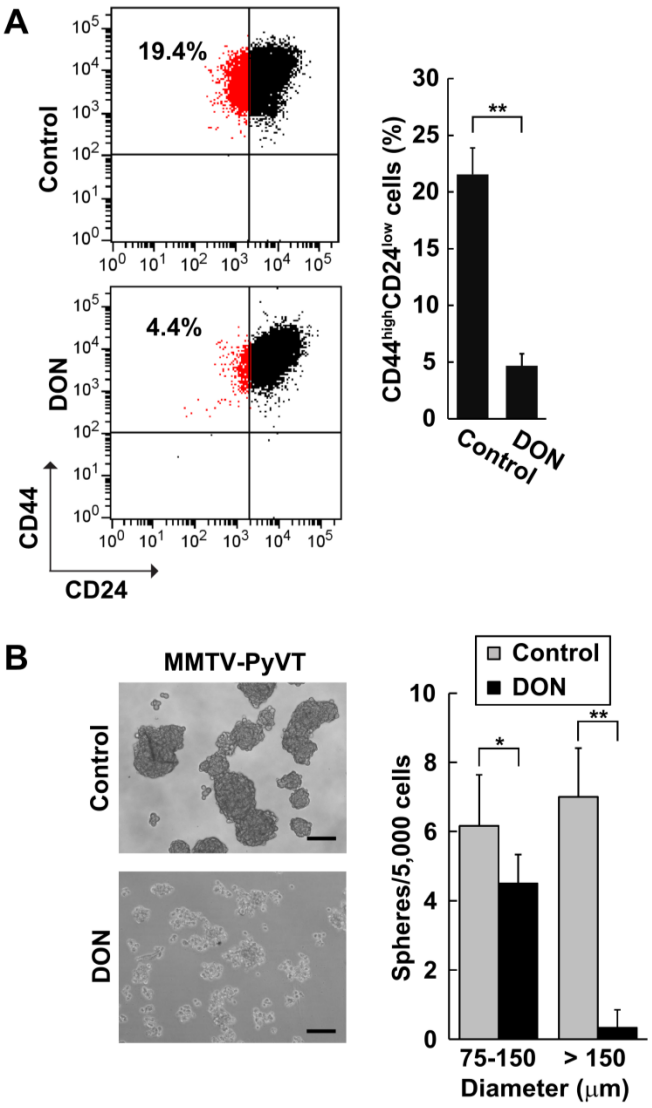

Figure 24. Disruption of HBP reduces the CSC-like properties in aggressive breast carcinoma cells. A MMTV-PyVT cells were treated with 20 μM DON (GFAT inhibitor) for 7 days. The $CD44^{high}/CD24^{low}$ subpopulations were estimated by flow cytometry. Data represent the mean ± S.D. of three independent experiments. **B** MMTV-PyVT cells were also examined for mammosphere formation. The 5,000 cells were seeded in a 24-well low-attachment plate and incubated with or without 20 μM DON for 7 days. Representative images of mammospheres were taken and mammosphere number was counted under a phase-contrast microscope. Spheres were classified into two groups according diameter: 75 – 150 and > 150 μm. Scale bar: 100 μm. Data represent the mean ± S.D. of six independent experiments. *, $p < 0.05$, **, $p < 0.01$ compared to untreated group.

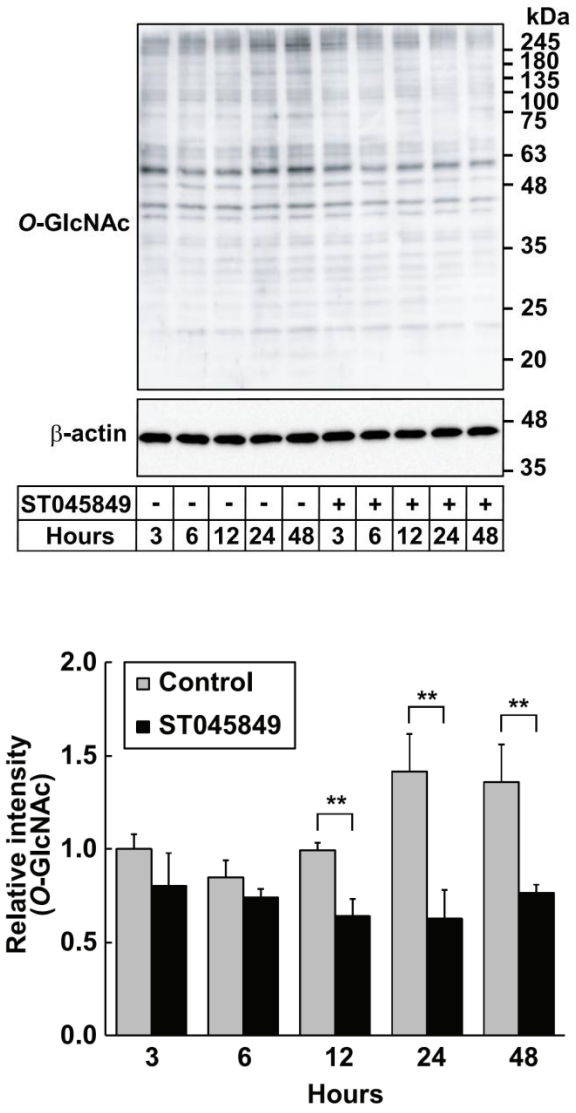

Figure 25. Pharmacology inhibitor of OGT reduces the protein *O*-GlcNAcylation levels. Protein *O*-GlcNAcylation levels after inhibition of OGT. MMTV-PyVT cancer cells were treated with 50 μM ST045849 (OGT inhibitor) for the indicated times (3–48 h). Whole cell lysate was detected *O*-GlcNAcylated proteins by western blot analysis. β-actin was used as an internal control. Band intensities were quantified by densitometric analysis using ImageJ software and standardized with respect to β-actin. Data represent the mean ± S.D. of three independent experiments. **, $p < 0.01$ versus control group.

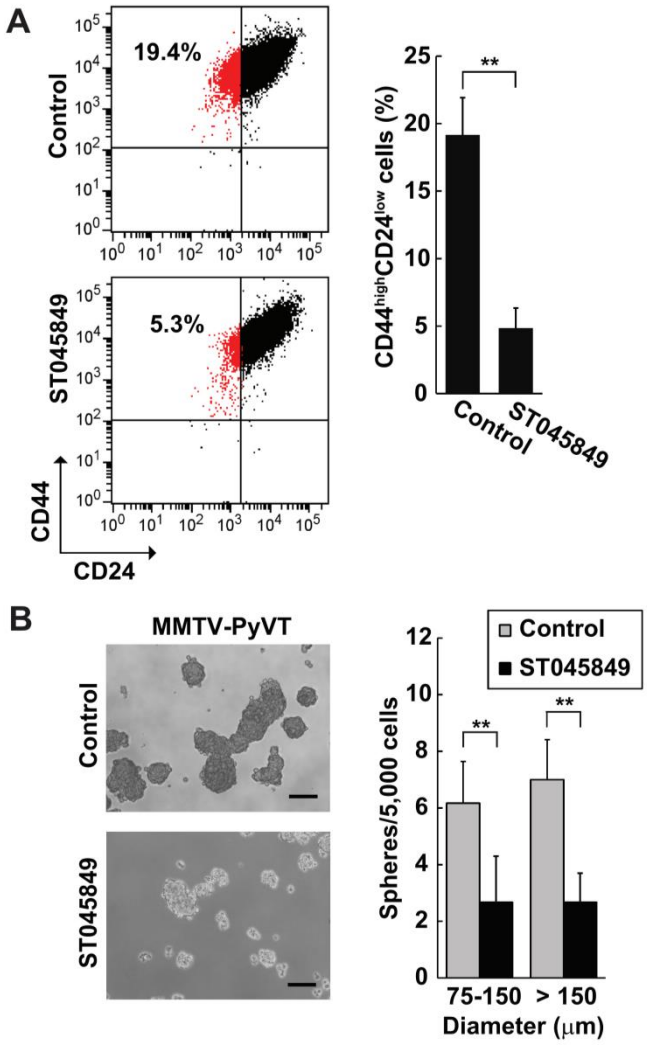

Figure 26. Significance of protein *O*-GlcNAcylation in the regulation of CSC-like properties. **A** Flow cytometric analysis of the $CD44^{high}/CD24^{low}$ subpopulation after pharmacological inhibition of protein *O*-GlcNAcylation. MMTV-PyVT cancer cells were treated with 50 μM ST045849 for 7 days. Treated cells were analyzed for CD24 and CD44 expression by flow cytometry. Data represent the mean ± S.D. of three independent experiments. **, $p < 0.01$ versus control. **B** Mammosphere formation after pharmacological inhibition of protein *O*-GlcNAcylation. MMTV-PyVT cancer cells were seeded into a 24-well low-attachment plate and treated with 50 μM ST045849 for 7 days. Representative images of mammospheres were taken and mammosphere number was counted under a phase-contrast microscope. Scale bar: 100 μm. Data represent the mean ± S.D. of three independent experiments. **, $p < 0.01$ versus control.

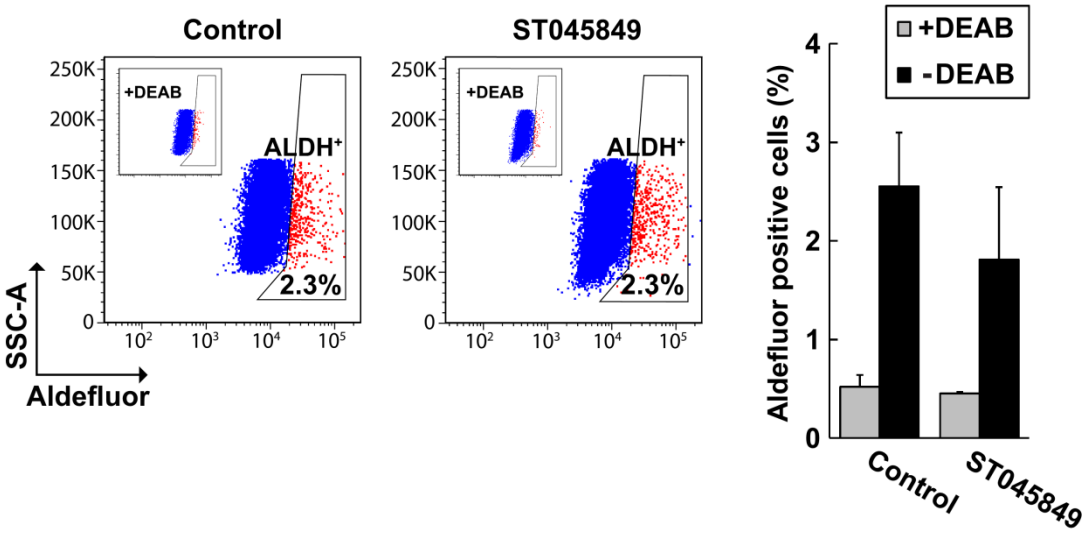

Figure 27. ALDH expression profiles after treatment with OGT inhibitor. MMTV-PyVT cells were treated with 50 µM ST045849 (OGT inhibitor) for 7 days. Treated cells were identified using a flow cytometry-based Aldefluor assay. Baseline fluorescence was established in the presence of DEAB (insets). Data represent the mean ± S.D. of four independent experiments.

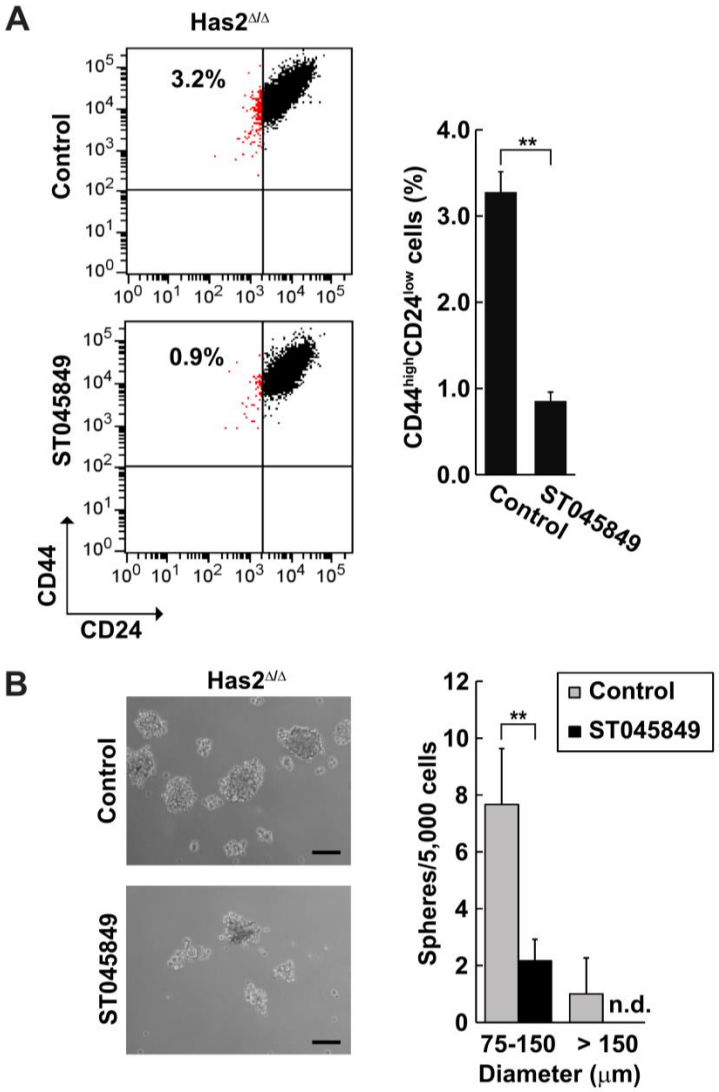

Figure 28. Inhibition of OGT promotes the reduction of CSC-like properties in Has2-deficient cells. A Has2-deficient Has2$^{\Delta/\Delta}$ cells were treated with 50 μM ST045849 for 7 days and analyzed for CD24 and CD44 expression by flow cytometry. Data represent the mean ± S.D. of three independent experiments. **, $p < 0.01$ versus untreated cells. **B** Mammosphere formation of Has2$^{\Delta/\Delta}$ cells treated with OGT inhibitor. Has2-deficient Has2$^{\Delta/\Delta}$ cells were seeded into 24-well low-attachment plate and treated with 50 μM ST045849 for 7 days. Representative images of mammospheres were taken and mammosphere number was counted under a phase-contrast microscope. Scale bar: 100 μm. Data represent the mean ± S.D. of six independent experiments. n.d.; not detected. **, $p < 0.01$ versus untreated cells.

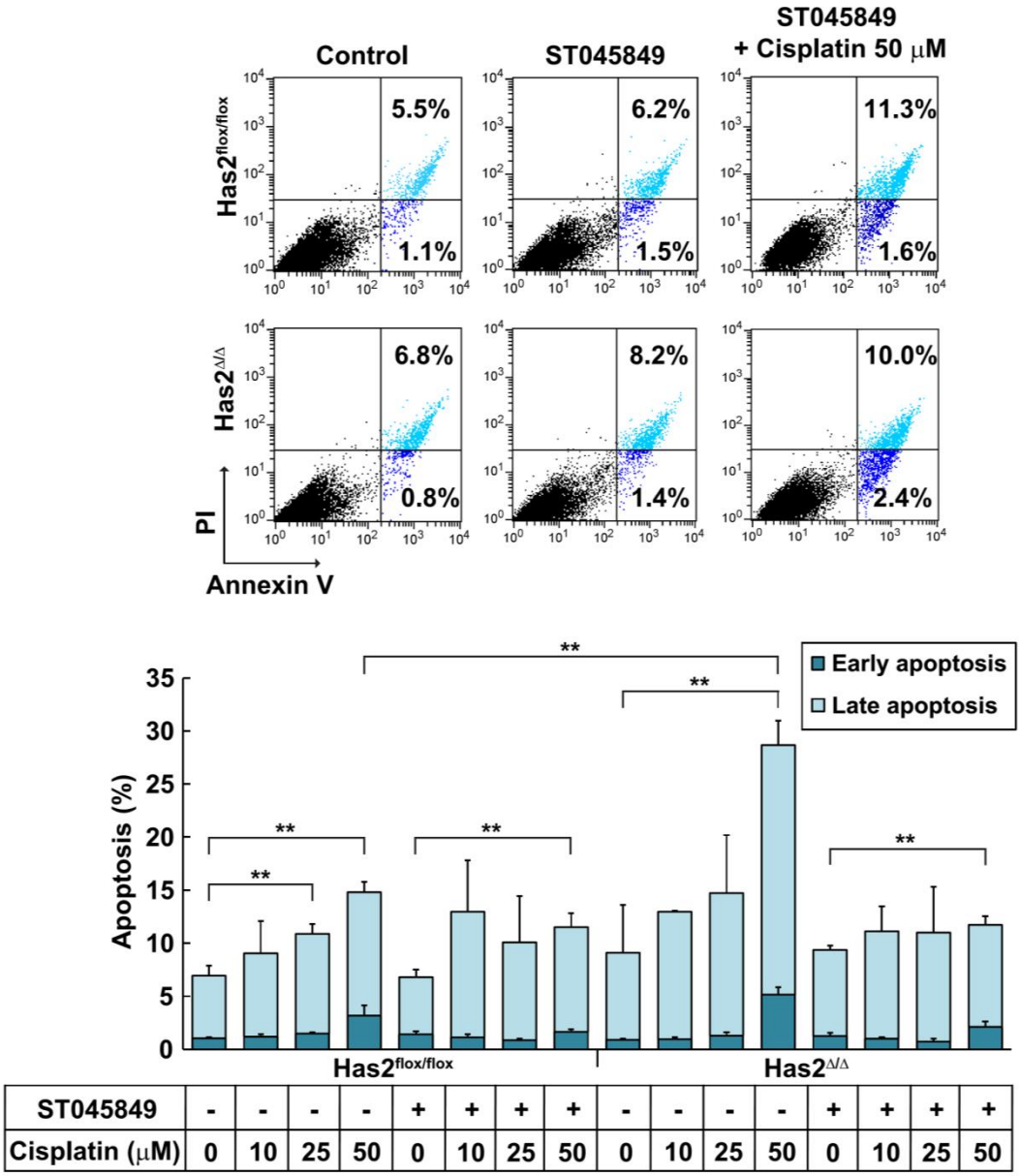

Figure 29. HA and *O*-GlcNAcylation signaling pathways play overlapping but distinct roles in the regulation of CSC-like phenotypes. Cisplatin-induced apoptosis in Has2-deficient $Has2^{\Delta/\Delta}$ and control $Has2^{flox/flox}$ cells. Cells were treated with 50 μM ST045849 alone or in combination with cisplatin (0-50 μM) for 16 h. Treated cells were stained with fluorescent Annexin V and PI and then analyzed by flow cytometry. Early and late apoptotic cells were represented as Annexin V^+/PI^- or Annexin V^+/PI^+ subpopulation, respectively. Data represent the mean ± S.D. of three independent experiments. **, $p < 0.01$.

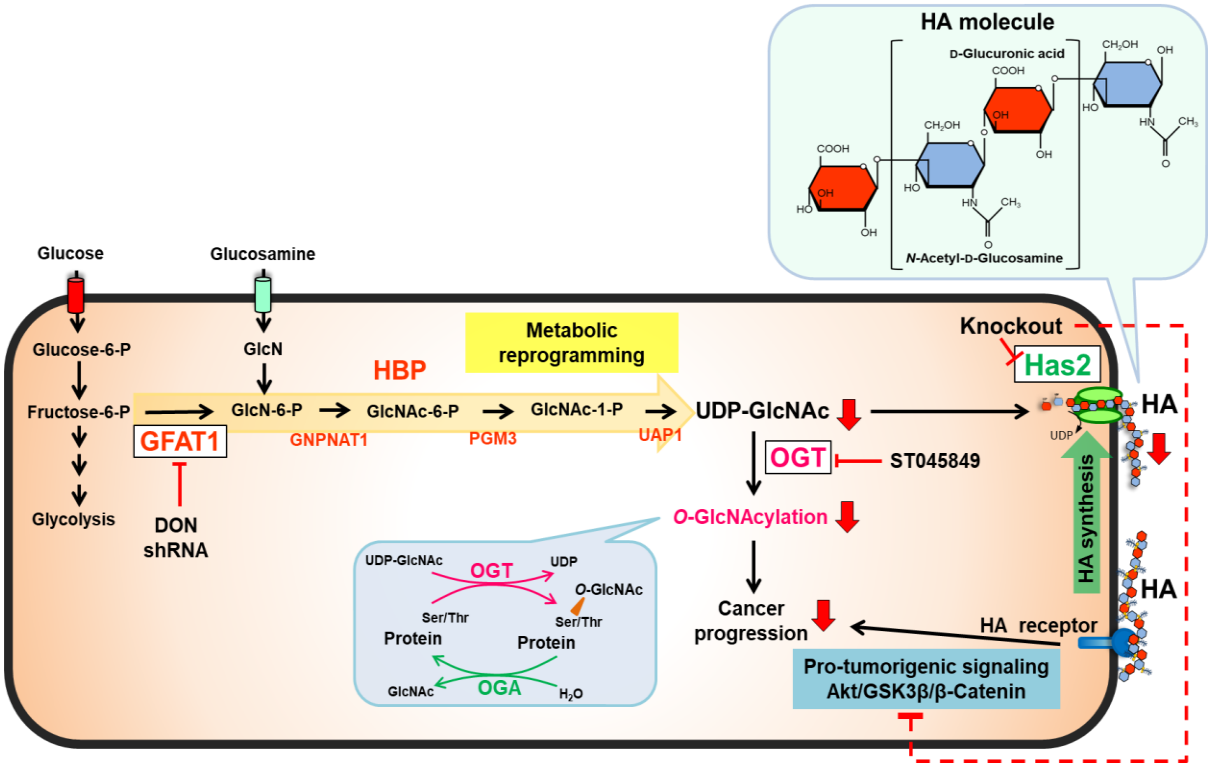

Figure 30. Schematic showing the HBP flux regulates signaling networks involved in HA production and protein *O*-GlcNAcylation promoting breast cancer progression. Enhanced HBP flux increased the levels of protein *O*-GlcNAcylation and HA production by providing UDP-GlcNAc. Has2 utilizes UDP-GlcNAc and UDP-GlcUA as substrates to produce HA molecules and then secreted them into the extracellular space. Upon binding to its receptor, the HA molecule may trigger the Akt/GSK3β/β-Catenin signaling pathway. Has2 deficiency impaired the protumorigenic signals and thereby suppressed the CSC-like properties. Furthermore, UDP-GlcNAc is also utilized for protein *O*-GlcNAcylation by OGT. Inhibition of HBP by either pharmacology DON inhibitor or shRNA against GFAT1, reduced *O*-GlcNAcylation, HA production and CSC-like properties. Suppression of protein *O*-GlcNAcylation, a downstream of HBP, with OGT inhibitor (ST045849), significantly decreased CSCs population in aggressive breast cancer cells.

Acknowledgement

Firstly, I would like to express my deepest gratitude to my advisor Prof. Dr. Naoki Itano for giving me an opportunity to start the PhD journey at Kyoto Sangyo University. Thank you for your hard work for grant applications and all your valuable guidance both in the experiments and writing dissertation.

I would like to thank to all lab members who have helped me preparing the reagents and did some experiments. I also would like to express my sincere appreciation to Assist. Prof. Dr. Tomomi Izumikawa and Assist. Prof. Dr. Takashi Kobayashi for all their helping. Thank you so much for your technical advice, guidance, encouragement and helpful discussion. This thesis would not have been success without their helping.

I would like to sincerely thank to Prof. Dr. Prachya Kongtaweelert and Prof. Dr. Siriwan Ong-chai who kindly gave me the advice, along with the members in Thailand Excellence Center for Tissue Engineering and Stem Cells, Chiang Mai University, Thailand. I would like to say thank so much to Dr. Theerawut Chanmee and Dr. Pawared Ontong who always gave me advices. I gratefully acknowledge the funding agencies including Heiwa Nakajima Foundation and Shoji Kawashima Memorial Scholarship Fund which provided the financial support during my PhD study.

Last but not least, my PhD would not have been achieved without my loved family. Thank you for your love, encouragement, and believing in me no matter what happens. Thank you for always being there.

Chatchadawalai Chokchaitaweesuk

References

1. Anttila, M.A., Tammi, R.H., Tammi, M.I., Syrjanen, K.J., Saarikoski, S.V., Kosma, V.M., 2000. High levels of stromal hyaluronan predict poor disease outcome in epithelial ovarian cancer. Cancer Res. 60(1), 150-155.
2. Auvinen, P., Rilla, K., Tumelius, R., Tammi, M., Sironen, R., Soini, Y., *et al*. 2014. Hyaluronan synthases (HAS1-3) in stromal and malignant cells correlate with breast cancer grade and predict patient survival. Breast Cancer Res Treat. 143(2), 277-286.
3. Auvinen, P., Tammi, R., Parkkinen, J., Tammi, M., Agren, U., Johansson, R., *et al*. 2000. Hyaluronan in peritumoral stroma and malignant cells associates with breast cancer spreading and predicts survival. Am J Pathol. 156(2), 529-536.
4. Bond, M.R., Hanover, J.A., 2015. A little sugar goes a long way: the cell biology of *O*-GlcNAc. J Biol Chem. 208(7). 869-880.
5. Bourguignon, L.Y.W., Earle, C., Shiina, M., 2017. Activation of Matrix Hyaluronan-Mediated CD44 Signaling, Epigenetic Regulation and Chemoresistance in Head and Neck Cancer Stem Cells. Int J Mol Sci. 18(9).
6. Bruntz, R.C., Lane, A.N., Higashi, R.M., Fan, T.W., 2017. Exploring cancer metabolism using stable isotope-resolved metabolomics (SIRM). J Biol Chem. 292(28), 11601-11609.
7. Cerami, E., Gao, J., Dogrusoz, U., Gross, B.E., Sumer, S.O., Aksoy, B.A., *et al*. 2012. The cBio cancer genomics portal: an open platform for exploring multidimensional cancer genomics data. Cancer Discov. 2(5), 401-404.
8. Chanmee, T., Ontong, P., Izumikawa, T., Higashide, M., Mochizuki, N., Chokchaitaweesuk, C., *et al*. 2016. Hyaluronan Production Regulates Metabolic and Cancer Stem-like Properties of Breast Cancer Cells via Hexosamine Biosynthetic Pathway-coupled HIF-1 Signaling. J Biol Chem. 291(46), 24105-24120.
9. Chanmee, T., Ontong, P., Kimata, K., Itano, N., 2015. Key Roles of Hyaluronan and Its

CD44 Receptor in the Stemness and Survival of Cancer Stem Cells. Front Oncol. 5, 180.

10. Chanmee, T., Ontong, P., Mochizuki, N., Kongtawelert, P., Konno, K., Itano, N., 2014. Excessive hyaluronan production promotes acquisition of cancer stem cell signatures through the coordinated regulation of Twist and the transforming growth factor beta (TGF-beta)-Snail signaling axis. J Biol Chem. 289(38), 26038-26056.
11. Cheung, W.D., Hart, G.W., 2008. AMP-activated protein kinase and p38 MAPK activate *O*-GlcNAcylation of neuronal proteins during glucose deprivation. J Biol Chem. 283(19), 13009-13020.
12. Chiaradonna, F., Ricciardiello, F., Palorini, R., 2018. The Nutrient-Sensing Hexosamine Biosynthetic Pathway as the Hub of Cancer Metabolic Rewiring. Cells. 7(6), E53.
13. Curtis, C., Shah, S.P., Chin, S.F., Turashvili, G., Rueda, O.M., Dunning, M.J., *et al*. 2012. The genomic and transcriptomic architecture of 2,000 breast tumours reveals novel subgroups. Nature. 486(7403), 346-352.
14. Dong, C., Yuan, T., Wu, Y., Wang, Y., Fan, T.W., Miriyala, S., *et al*. 2013. Loss of FBP1 by Snail-mediated repression provides metabolic advantages in basal-like breast cancer. Cancer Cell. 23(3), 316-331.
15. Dontu, G., Abdallah, W.M., Foley, J.M., Jackson, K.W., Clarke, M.F., Kawamura, M.J., *et al*. 2003. In vitro propagation and transcriptional profiling of human mammary stem/progenitor cells. Genes & development. 17(10), 1253-1270.
16. Dontu, G., Jackson, K.W., McNicholas, E., Kawamura, M.J., Abdallah, W.M., Wicha, M.S., 2004. Role of Notch signaling in cell-fate determination of human mammary stem/progenitor cells. Breast Cancer Res. 6(6), R605-615.
17. Ellrott, K., Bailey, M.H., Saksena, G., Covington, K.R., Kandoth, C., Stewart, C., *et al*. 2018. Scalable Open Science Approach for Mutation Calling of Tumor Exomes Using Multiple Genomic Pipelines. Cell Syst. (3)6, 271-281.

18. Finak, G., Bertos, N., Pepin, F., Sadekova, S., Souleimanova, M., Zhao, H., *et al*. 2008. Stromal gene expression predicts clinical outcome in breast cancer. Nat Med. 14(5), 518-527.
19. Gao, Q., Liang, W.-W., Foltz, S.M., Mutharasu, G., Jayasinghe, R.G., Cao, S., *et al*. 2018. Driver Fusions and Their Implications in the Development and Treatment of Human Cancers. Cell Rep. 23(1), 227-238.
20. Glück, S., Ross, J.S., Royce, M., McKenna, E.F., Jr., Perou, C.M., *et al*. 2012. TP53 genomics predict higher clinical and pathologic tumor response in operable early-stage breast cancer treated with docetaxel-capecitabine +/- trastuzumab. Breast Cancer Res Treat. 132(3), 781-791.
21. Gohr, K., Hamacher, A., Engelke, L.H., Kassack, M.U., 2017. Inhibition of PI3K/Akt/mTOR overcomes cisplatin resistance in the triple negative breast cancer cell line HCC38. BMC Cancer. 17(1), 711.
22. Grimshaw, M.J., Cooper, L., Papazisis, K., Coleman, J.A., Bohnenkamp, H.R., Chiapero-Stanke, L., *et al*. 2008. Mammosphere culture of metastatic breast cancer cells enriches for tumorigenic breast cancer cells. Breast Cancer Res. 10(3), R52.
23. Groves, J.A., Lee, A., Yildirir, G., Zachara, N.E., 2013. Dynamic *O*-GlcNAcylation and its roles in the cellular stress response and homeostasis. Cell Stress Chaperones. 18(5), 535–558.
24. Guy, C.T., Cardiff, R.D., Muller, W.J., 1992a. Induction of mammary tumors by expression of polyomavirus middle T oncogene: a transgenic mouse model for metastatic disease. Mol Cell Biol. 12(3), 954-961.
25. Guy, C.T., Webster, M.A., Schaller, M., Parsons, T.J., Cardiff, R.D., Muller, W.J., 1992b. Expression of the neu protooncogene in the mammary epithelium of transgenic mice induces metastatic disease. Proc Natl Acad Sci USA. 89(22). 10578-10582.

26. Hart, G.W., 2014. Minireview series on the thirtieth anniversary of research on *O*-GlcNAcylation of nuclear and cytoplasmic proteins: Nutrient regulation of cellular metabolism and physiology by *O*-GlcNAcylation. J Biol Chem. 289(50), 34422-34423.
27. Heldin, P., Lin, C.Y., Kolliopoulos, C., Chen, Y.H., Skandalis, S.S., 2018. Regulation of hyaluronan biosynthesis and clinical impact of excessive hyaluronan production. Matrix Biol.
28. Hoadley, K.A., Yau, C., Hinoue, T., Wolf, D.M., Lazar, A.J., Drill, E., *et al*. 2018. Cell-of-Origin Patterns Dominate the Molecular Classification of 10,000 Tumors from 33 Types of Cancer. Cell. 173(2), 291-304.
29. Itano, N., Sawai, T., Yoshida, M., Lenas, P., Yamada, Y., Imagawa, M., *et al*. 1999. Three isoforms of mammalian hyaluronan synthases have distinct enzymatic properties. J Biol Chem. 274(35), 25085-25092.
30. Itkonen, H.M., Engedal, N., Babaie, E., Luhr, M., Guldvik, I.J., Minner, S., *et al*. 2015. UAP1 is overexpressed in prostate cancer and is protective against inhibitors of *N*-linked glycosylation. Oncogene. 34(28), 3744-3750.
31. Ito, K., Suda, T., 2014. Metabolic requirements for the maintenance of self-renewing stem cells. Nat Rev Mol Cell Biol. 15(4), 243-256.
32. Janku, F., Yap, T.A., Meric-Bernstam, F., 2018. Targeting the PI3K pathway in cancer: are we making headway? Nat Rev Clin Oncol. 15(5), 273-291.
33. Jokela, T.A., Makkonen, K.M., Oikari, S., Kärnä, R., Koli, E., Hart, G.W., *et al*. 2011. Cellular content of UDP-*N*-acetylhexosamines controls hyaluronan synthase 2 expression and correlates with *O*-linked *N*-acetylglucosamine modification of transcription factors YY1 and SP1. J Biol Chem. 286(38), 33632-33640.
34. Kanda, Y., 2013. Investigation of the freely available easy-to-use software 'EZR' for medical statistics. Bone Marrow Transplant. 48(3), 452-458.

35. Karnoub, A.E., Dash, A.B., Vo, A.P., Sullivan, A., Brooks, M.W., Bell, G.W., *et al*. 2007. Mesenchymal stem cells within tumour stroma promote breast cancer metastasis. Nature. 449(7162), 557-563.
36. Kobayashi, N., Miyoshi, S., Mikami, T., Koyama, H., Kitazawa, M., Takeoka, M., *et al*. 2010. Hyaluronan deficiency in tumor stroma impairs macrophage trafficking and tumor neovascularization. Cancer Res. 70(18), 7073-7083.
37. Koyama, H., Hibi, T., Isogai, Z., Yoneda, M., Fujimori, M., Amano, J., *et al*. 2007. Hyperproduction of hyaluronan in neu-induced mammary tumor accelerates angiogenesis through stromal cell recruitment: possible involvement of versican/PG-M. Am J Pathol. 170(3), 1086-1099.
38. Koyama, H., Kobayashi, N., Harada, M., Takeoka, M., Kawai, Y., Sano, K., *et al*. 2008. Significance of tumor-associated stroma in promotion of intratumoral lymphangiogenesis: pivotal role of a hyaluronan-rich tumor microenvironment. Am J Pathol. 172(1), 179-193.
39. Kreppel, L.K., Hart, G.W., 1999. Regulation of a cytosolic and nuclear *O*-GlcNAc transferase. Role of the tetratricopeptide repeats. J Biol Chem. 274(45), 32015-32022.
40. Lawlor, E.R., Scheel, C., Irving, J., Sorensen, P.H., 2002. Anchorage-independent multi-cellular spheroids as an in vitro model of growth signaling in Ewing tumors. Oncogene. 21(2), 307-318.
41. Lefebvre, C., Bachelot, T., Filleron, T., Pedrero, M., Campone, M., Soria, J.C., *et al*. 2016. Mutational Profile of Metastatic Breast Cancers: A Retrospective Analysis. PLoS Med. 13(12), e1002201.
42. Liu, J., Lichtenberg, T., Hoadley, K.A., Poisson, L.M., Lazar, A.J., Cherniack, A.D., *et al*. 2018. An Integrated TCGA Pan-Cancer Clinical Data Resource to Drive High-Quality Survival Outcome Analytics. Cell. 173(2), 400-416.
43. Luo, J., 2009. Glycogen synthase kinase 3beta (GSK3beta) in tumorigenesis and cancer

chemotherapy. Cancer Lett. 273(2), 194-200.

44. Ma, I., Allan, A.L., 2011. The role of human aldehyde dehydrogenase in normal and cancer stem cells. Stem Cell Res Rep. 7(2), 292-306.
45. Ma, X.J., Dahiya, S., Richardson, E., Erlander, M. & Sgroi, D.C. 2009. Gene expression profiling of the tumor microenvironment during breast cancer progression. Breast Cancer Res. 11(1), R7.
46. Martelli, A.M., Evangelisti, C., Chiarini, F., Grimaldi, C., McCubrey, J.A., 2010. The emerging role of the phosphatidylinositol 3-kinase/akt/mammalian target of rapamycin signaling network in cancer stem cell biology. Cancers (Basel). 2(3), 1576-1596.
47. Menendez, J.A., Joven, J., Cufi, S., Corominas-Faja, B., Oliveras-Ferraros, C., Cuyas, E., *et al*. 2013. The Warburg effect version 2.0: metabolic reprogramming of cancer stem cells. Cell Cycle. 12(8), 1166-1179.
48. Nakajima, K., Kitazume, S., Angata, T., Fujinawa, R., Ohtsubo, K., Miyoshi, E., *et al*. 2010. Simultaneous determination of nucleotide sugars with ion-pair reversed-phase HPLC. Glycobiology. 20(7), 865-871.
49. Ohno, Y., Shingyoku, S., Miyake, S., Tanaka, A., Fudesaka, S., Shimizu, Y., *et al*. 2018. Differential regulation of the sphere formation and maintenance of cancer-initiating cells of malignant mesothelioma via CD44 and ALK4 signaling pathways. Oncogene. 37(49), 6357-6367.
50. Oikari, S., Kettunen, T., Tiainen, S., Hayrinen, J., Masarwah, A., Sudah, M., *et al*. 2018. UDP-sugar accumulation drives hyaluronan synthesis in breast cancer. Matrix Biol. 67, 63-74.
51. Okuda, H., Kobayashi, A., Xia, B., Watabe, M., Pai, S.K., Hirota, S., *et al*. 2012. Hyaluronan synthase HAS2 promotes tumor progression in bone by stimulating the interaction of breast cancer stem-like cells with macrophages and stromal cells. Cancer

Res. 72(2), 537-547.

52. Ontong, P., Hatada, Y., Taniguchi, S., Kakizaki, I., Itano, N., 2014. Effect of a cholesterol-rich lipid environment on the enzymatic activity of reconstituted hyaluronan synthase. Biochem Biophy Res Commun. 443(2), 666-671.
53. Pereira, B., Chin, S.F., Rueda, O.M., Vollan, H.K., Provenzano, E., Bardwell, H.A., *et al*. 2016. The somatic mutation profiles of 2,433 breast cancers refines their genomic and transcriptomic landscapes. Nat Commun. 7, 11479.
54. Prater, M., Shehata, M., Watson, C.J., Stingl, J., 2013. Enzymatic dissociation, flow cytometric analysis, and culture of normal mouse mammary tissue. Methods Mol Biol. 946, 395-409.
55. Radvanyi, L., Singh-Sandhu, D., Gallichan, S., Lovitt, C., Pedyczak, A., Mallo, G., *et al*. 2005. The gene associated with trichorhinophalangeal syndrome in humans is overexpressed in breast cancer. Proc Natl Acad Sci USA. 102(31), 11005-11010.
56. Rhodes, D.R., Kalyana-Sundaram, S., Mahavisno, V., Varambally, R., Yu, J., Briggs, B.B., *et al*. 2007. Oncomine 3.0: genes, pathways, and networks in a collection of 18,000 cancer gene expression profiles. Neoplasia. 9(2), 166-180.
57. Rhodes, D.R., Yu, J., Shanker, K., Deshpande, N., Varambally, R., Ghosh, D., *et al*. 2004. ONCOMINE: a cancer microarray database and integrated data-mining platform. Neoplasia. 6(1), 1-6.
58. Richardson, A.L., Wang, Z.C., De Nicolo, A., Lu, X., Brown, M., Miron, A., *et al*. 2006. X chromosomal abnormalities in basal-like human breast cancer. Cancer Cell. 9(2), 121-132.
59. Ropponen, K., Tammi, M., Parkkinen, J., Eskelinen, M., Tammi, R., Lipponen, P., *et al*. 1998. Tumor cell-associated hyaluronan as an unfavorable prognostic factor in colorectal cancer. Cancer Res. 58(2), 342-347.

60. Sanchez-Vega, F., Mina, M., Armenia, J., Chatila, W.K., Luna, A., La, K.C., *et al*. 2018. Oncogenic Signaling Pathways in The Cancer Genome Atlas. Cell. 173(2), 321-337.

61. Slawson, C., Hart, G.W., 2011. *O*-GlcNAc signalling: implications for cancer cell biology. Nat Rev Cancer. 11(9), 678-684.

62. Soga, T., 2013. Cancer metabolism: key players in metabolic reprogramming. Cancer Sci. 104(3). 275-281.

63. Sørlie, T., Perou, C.M., Tibshirani, R., Aas, T., Geisler, S., Johnsen, H., *et al*. 2001. Gene expression patterns of breast carcinomas distinguish tumor subclasses with clinical implications. Proc Natl Acad Sci USA. 98(19), 10869-10874.

64. Sørlie, T., Tibshirani, R., Parker, J., Hastie, T., Marron, J.S., Nobel, A., *et al*. 2003. Repeated observation of breast tumor subtypes in independent gene expression data sets. Proc Natl Acad Sci USA. 100(14), 8418-8423.

65. Taparra, K., Tran, P.T., Zachara, N.E., 2016. Hijacking the Hexosamine Biosynthetic Pathway to Promote EMT-Mediated Neoplastic Phenotypes. Front Oncol. 6, 85.

66. Taylor, A.M., Shih, J., Ha, G., Gao, G.F., Zhang, X., Berger, A.C., *et al*. 2018. Genomic and Functional Approaches to Understanding Cancer Aneuploidy. Cancer Cell. 33(4), 676-689.

67. Taylor, R.P., Parker, G.J., Hazel, M.W., Soesanto, Y., Fuller, W., Yazzie, M.J., *et al*. 2008. Glucose deprivation stimulates *O*-GlcNAc modification of proteins through up-regulation of *O*-linked *N*-acetylglucosaminyltransferase. J Biol Chem. 283(10), 6050-6057.

68. TCGA (The Cancer Genome Atlas). The Cancer Genome Atlas - Invasive Breast Carcinoma Gene Expression Data. http://tcga-data.nci.nih.gov/tcga/

69. Toole, B.P., 2004. Hyaluronan: from extracellular glue to pericellular cue. Nat Rev Cancer. 4(7), 528-539.

70. Turashvili, G., Bouchal, J., Baumforth, K., Wei, W., Dziechciarkova, M., Ehrmann, J., *et al*. 2007. Novel markers for differentiation of lobular and ductal invasive breast carcinomas by laser microdissection and microarray analysis. BMC Cancer. 7, 55.

71. Vander Heiden, M.G., Cantley, L.C., Thompson, C.B., 2009. Understanding the Warburg effect: the metabolic requirements of cell proliferation. Science. 324(5930). 1029-1033.

72. Vigetti, D., Deleonibus, S., Moretto, P., Bowen, T., Fischer, J.W., Grandoch, M., *et al*. 2014. Natural antisense transcript for hyaluronan synthase 2 (HAS2-AS1) induces transcription of HAS2 via protein *O*-GlcNAcylation. J Biol Chem. 289(42), 28816-28826.

73. Warburg, O., 1956. On the origin of cancer cells. Science. 123(3191), 309-314.

74. Weinstein, J.N., Collisson, E.A., Mills, G.B., Shaw, K.R., Ozenberger, B.A., Ellrott, K., *et al*. 2013. The Cancer Genome Atlas Pan-Cancer analysis project. Nat Genet. 45(10), 1113-1120.

75. Wu, G., He, X., 2006. Threonine 41 in beta-catenin serves as a key phosphorylation relay residue in beta-catenin degradation. Biochemistry. 45(16), 5319-5323.

76. Xu, X., Chai, S., Wang, P., Zhang, C., Yang, Y., Yang, Y., *et al*. 2015. Aldehyde dehydrogenases and cancer stem cells. Cancer Lett. 369(1), 50-57.

77. Zhao, H., Langerod, A., Ji, Y., Nowels, K.W., Nesland, J.M., Tibshirani, R., *et al*. 2004. Different gene expression patterns in invasive lobular and ductal carcinomas of the breast. Mol Biol Cell. 15(6), 2523-2536.